

Climate-Change Controls on River Delta Avulsion Location and Frequency

 A. J. Chadwick^{1,2}  and M. P. Lamb¹ 
¹Division of Geological and Planetary Sciences, California Institute of Technology, Pasadena, CA, USA, ²Department of Earth and Environmental Sciences & St. Anthony Falls Laboratory, University of Minnesota, Minneapolis, MN, USA

Key Points:

- Sea-level rise causes more frequent river avulsions at a location relative to the shoreline set by backwater hydrodynamics
- Increases in upstream sediment supply can trigger avulsions upstream of the backwater zone
- Increases in flood frequency cause erosion in the backwater zone, reducing long-term aggradation rate and avulsion frequency

Supporting Information:

Supporting Information may be found in the online version of this article.

Correspondence to:

A. J. Chadwick,
achadwic@umn.edu

Citation:

Chadwick, A. J., & Lamb, M. P. (2021). Climate-change controls on river delta avulsion location and frequency. *Journal of Geophysical Research: Earth Surface*, 126, e2020JF005950. <https://doi.org/10.1029/2020JF005950>

Received 10 NOV 2020
 Accepted 18 MAY 2021

Abstract Coastal rivers that build deltas undergo repeated avulsion events—that is, abrupt changes in river course—which we need to understand to predict land building and flood hazards in coastal landscapes. Climate change can impact water discharge, flood frequency, sediment supply, and sea level, all of which could impact avulsion location and frequency. Here we present results from quasi-2D morphodynamic simulations of repeated delta-lobe construction and avulsion to explore how avulsion location and frequency are affected by changes in relative sea level, sediment supply, and flood regime. Model results indicate that relative sea-level rise drives more frequent avulsions that occur at a distance from the shoreline set by backwater hydrodynamics. Reducing the sediment supply relative to transport capacity has little impact on deltaic avulsions, because, despite incision in the upstream trunk channel, deltas can still aggrade as a result of progradation. However, increasing the sediment supply relative to transport capacity can shift avulsions upstream of the backwater zone because aggradation in the trunk channel outpaces progradation-induced delta aggradation. Increasing frequency of overbank floods causes less frequent avulsions because floods scour the riverbed within the backwater zone, slowing net aggradation rates. Results provide a framework to assess upstream and downstream controls on avulsion patterns over glacial-interglacial cycles, and the impact of land use and anthropogenic climate change on deltas.

1. Introduction

River deltas are densely populated, ecologically diverse, and socioeconomically valuable landscapes (Gleick, 2003; Olson & Dinerstein, 1998; Vörösmarty et al., 2009) that are sensitive to changes in climate (Bianchi & Allison, 2009; Giosan, 2014; Syvitski, 2008). Previous work has identified three primary influences of climate on delta growth, namely 1) changes in sea level, 2) changes in sediment supply and transport capacity, and 3) changes in flood regime (Blum & Törnqvist, 2000; Hallet et al., 1996; Langbein & Schumm, 1958; Members, 1988; Walling & Webb, 1996). However, little is known about how these changes might affect the occurrence of channel avulsions, i.e., catastrophic shifts in river course to the shoreline (Ganti et al., 2014; Mohrig et al., 2000; Slingerland & Smith, 2004). River avulsions are a fundamental process responsible for building delta lobes, and tend to occur at a characteristic location and frequency for each delta (Figures 1a and 1b). Understanding where and when avulsions will occur in response to climate change is crucial for predicting future flood hazards and sustaining land for coastal cities and ecosystems.

At the downstream boundary of deltas, climate-induced sea-level changes impact delta growth and retreat (Stanley & Warne, 1994). Field observations show sea-level rise enhances aggradation in the lower reaches of deltaic rivers (Fisk, 1945; Powell, 1875; Schumm, 1993), a trend supported by laboratory experiments (Kim et al., 2006; Martin et al., 2009) and numerical models (Parker et al., 2008; Swenson et al., 2005). The avulsion frequency f_A has been found to scale inversely with the channel-filling timescale T_c (Figure 1c) (Jerolmack & Mohrig, 2007; Reitz & Jerolmack, 2012),

$$f_A \propto 1 / T_c \quad (1)$$

where $T_c = H_c / v_a$ is the time required to fill the channel of depth H_c at aggradation rate v_a (Figure 1d). Models also show a regime at low sea-level rise rates, where avulsion frequency is insensitive to sea-level rise because the rate of topset aggradation that drives avulsion is primarily controlled by sediment supply and delta progradation (Chadwick et al., 2019, 2020; Ratliff et al., 2018). At very high rise rates, avulsion frequency is expected to either reach an upper limit where nearly the entire sediment supply is deposited

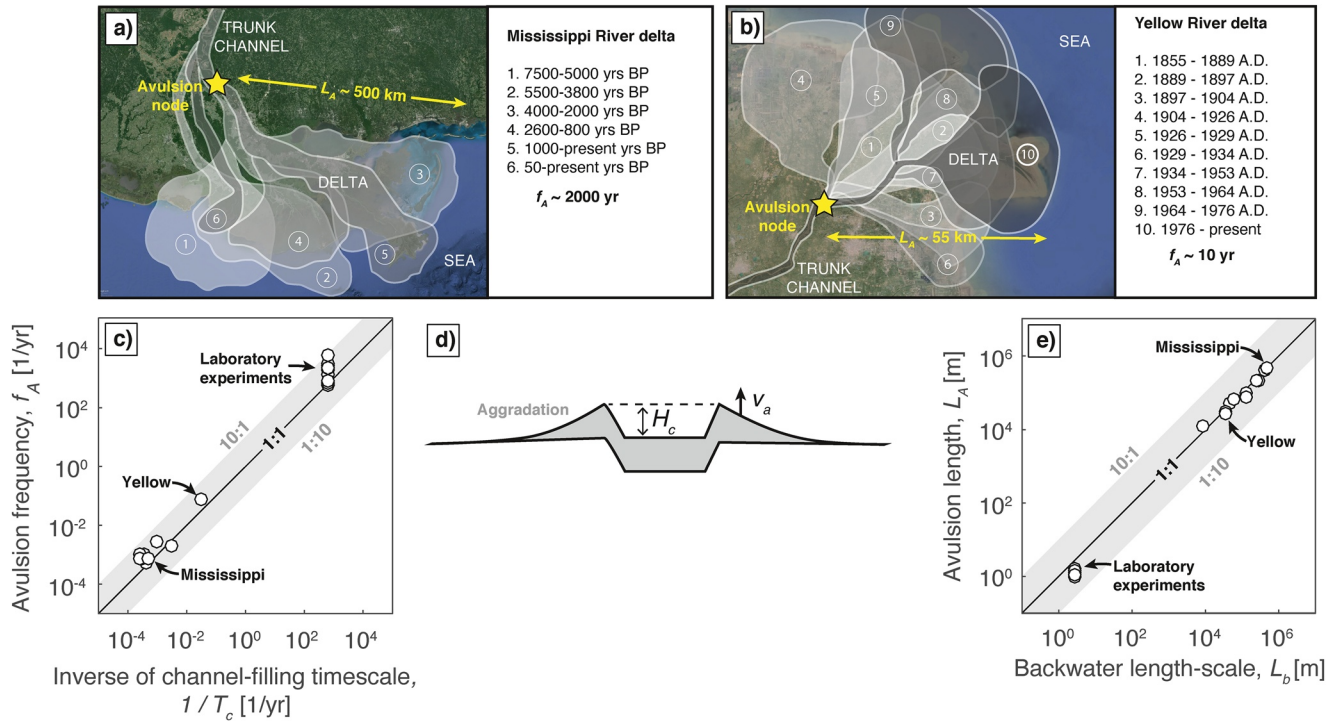


Figure 1. Mapped delta lobes of (a) the Mississippi River and (b) the Yellow River overlain on Google Earth imagery, showing characteristic avulsion length, L_A , and avulsion frequency, f_A (after Coleman et al., 1998 and Pang & Si, 1979). (c) Scaling relationship between measured avulsion frequency and the inverse of the channel-filling timescale (Equation 1) (Ganti et al., 2014; Jerolmack & Mohrig, 2007). (d) Schematic channel cross section showing aggradation at rate v_a . Channel avulsion occurs when the river has aggraded to a critical height, comparable to the channel depth H_c , that renders it unstable (Ganti et al., 2014; Mohrig et al., 2000). (e) Scaling relationship between measured avulsion length and computed backwater length-scale (Equation 3) (Chatanantavet et al., 2012; Ganti, Chadwick, Hassenruck-Gudipati, Fuller, et al., 2016; Ganti et al., 2014).

on the active delta topset (Chadwick et al., 2020) or avulsions do not occur because the entire delta is drowned (Muto, 2001; Muto et al., 2007; Parker et al., 2008; Tomer et al., 2011). Enhanced aggradation during sea-level rise has been linked to more frequent avulsions on the Rhine-Meuse delta (Stouthamer & Berendsen, 2001; Törnqvist, 1994) and in delta laboratory experiments (Martin et al., 2009). However, the Mitchell River delta provides a counterexample where avulsion frequency was reduced during Holocene sea-level rise (T. I. Lane et al., 2017).

Relative sea-level rise can also affect avulsion locations, and thereby set the location of the delta apex. On fan deltas, avulsions typically occur at a topographic slope break tied to a canyon outlet or bedrock-alluvial transition (Ganti et al., 2014; Muto et al., 2016), which may be approximated as geographically fixed in simplified models (Jerolmack, 2009). Fan delta size—characterized by the distance L_A between the delta apex, or avulsion node, and the shoreline—approaches the autostratigraphic length-scale, L_{auto} (Muto et al., 2007),

$$L_A \sim L_{auto} \quad (2)$$

where $L_{auto} = q_s / \sigma$, q_s is width-averaged sediment supply, and σ is relative sea-level rise rate. L_{auto} represents the delta size when rise rate and aggradation rate are in equilibrium, assuming the entire sediment supply is deposited uniformly on the delta topset (i.e., $\sigma = v_a = q_s / L_A$). This equilibrium is not sustainable because part of the sediment supply is delivered to the delta foreset, which necessarily grows thicker as sea-level rises. As a result, the delta shrinks and eventually drowns, in a process known as autoretreat over timescales of $T_{auto} = \frac{L_{auto}^2 S}{q_s}$, where S is channel-bed slope (Muto, 2001; Muto et al., 2007; Parker et al., 2008; Tomer et al., 2011).

In contrast to fan deltas, lowland deltas commonly feature avulsion nodes on unconfined plains without a topographic slope break (Brooke et al., 2020; Ganti et al., 2014). Avulsion nodes on lowland deltas have been documented to shift with movement of the shoreline (Ganti, Chadwick, Hassenruck-Gudipati, Fuller, & Lamb, 2016; Ganti et al., 2014) to maintain a constant avulsion length L_A that scales with the backwater length-scale L_b (Figure 1e) (Chatanantavet et al., 2012; Jerolmack & Swenson, 2007),

$$L_A \propto L_b \quad (3)$$

where $L_b = H_c / S$ is the ratio of bankfull river channel depth, H_c , to channel-bed slope S (Lamb et al., 2012; Paola & Mohrig, 1996). Therefore, deltas with backwater-influenced avulsions might translate upstream, rather than reduce in size, with rising sea level (Chadwick et al., 2020; Moran et al., 2017).

Changes in water and sediment supply cause aggradation and incision on deltas, which might also affect avulsion frequency and location (Blum & Törnqvist, 2000; Schumm, 1993). Early experimental efforts showed higher sediment supply was associated with enhanced aggradation and greater avulsion frequency (Ashworth et al., 2004; Bryant et al., 1995). Similarly, the Rhine-Meuse delta had more frequent avulsions during a period of increased sediment supply in the Holocene (Stouthamer & Berendsen, 2001). Avulsion location may also be influenced by sediment supply, with pulses in sediment supply historically linked to avulsion sites far upstream of deltas, for example, on the Tacquari megafan (Makaske et al., 2012) and in New Zealand (Korup, 2004).

Climate change can also affect the magnitude and frequency of large flood events on river deltas (Knox, 2000; Members, 1988; Munoz et al., 2018). Flood regimes control the aggradation of both channel and floodplain (Leopold & Maddock, 1953; Naito & Parker, 2019), with potential consequences for river avulsion (Brizga & Finlayson, 1990; Hajek & Edmonds, 2014; Nicholas et al., 2018). For example, on deltas with flashier flood regimes, field evidence indicates that less in-channel aggradation is necessary to trigger an avulsion, resulting in more frequent avulsions (Ganti et al., 2014; Moodie et al., 2019) (Figure 1d).

Flood regimes can also affect avulsion location. Chatanantavet et al. (2012) hypothesized that variable flood discharges and non-uniform flow in the backwater zone (i.e., the reach within $\sim L_b$ of the shoreline) cause a spatial maximum in long-term aggradation rate that determined the avulsion site. Scaled physical experiments and subsequent modeling supported the backwater hypothesis, showing deltas produced a backwater-scaled avulsion node when subjected to variable flood regimes with subcritical Froude numbers (Chadwick et al., 2019; Ganti, Chadwick, Hassenruck-Gudipati, Fuller, et al., 2016; Ganti, Chadwick, Hassenruck-Gudipati, & Lamb, 2016). Numerical simulations have also isolated special cases where rapid sea-level rise (Chadwick et al., 2019; Moran et al., 2017; Wu et al., 2020) or the assumption of a horizontal deltaic floodplain (Chadwick et al., 2019; Ratliff et al., 2021) can give rise to backwater-scaled aggradation and avulsion without flood variability.

Here, we build on recent advances in modeling backwater-driven avulsions on deltas (Chadwick et al., 2020; Chatanantavet et al., 2012; Moodie et al., 2019; Moran et al., 2017; Ratliff et al., 2018) to better understand the effect of climate change on avulsion frequency and location. We use the model of Chadwick et al. (2019) that includes backwater hydrodynamics, variable flood discharges, and multiple deltaic lobes that are abandoned and reoccupied due to avulsion. Previous work used the model to address the origin of a backwater-scaled avulsion node (Chadwick et al., 2019), and the effect of relative sea-level rise on avulsion frequency (Chadwick et al., 2020). Here we present new results to explore the effect of sea-level rise on avulsion location, and the roles of sediment supply and flood regime on avulsion frequency and location. First, we briefly review the model and how climate forcing is parameterized. We then present results from numerical simulations with systematic variation of climate forcing, exploring systematic change in avulsion location and frequency as well as autogenic variability. Finally, we discuss implications for avulsion dynamics over glacial-interglacial cycles and during modern anthropogenic climate change.

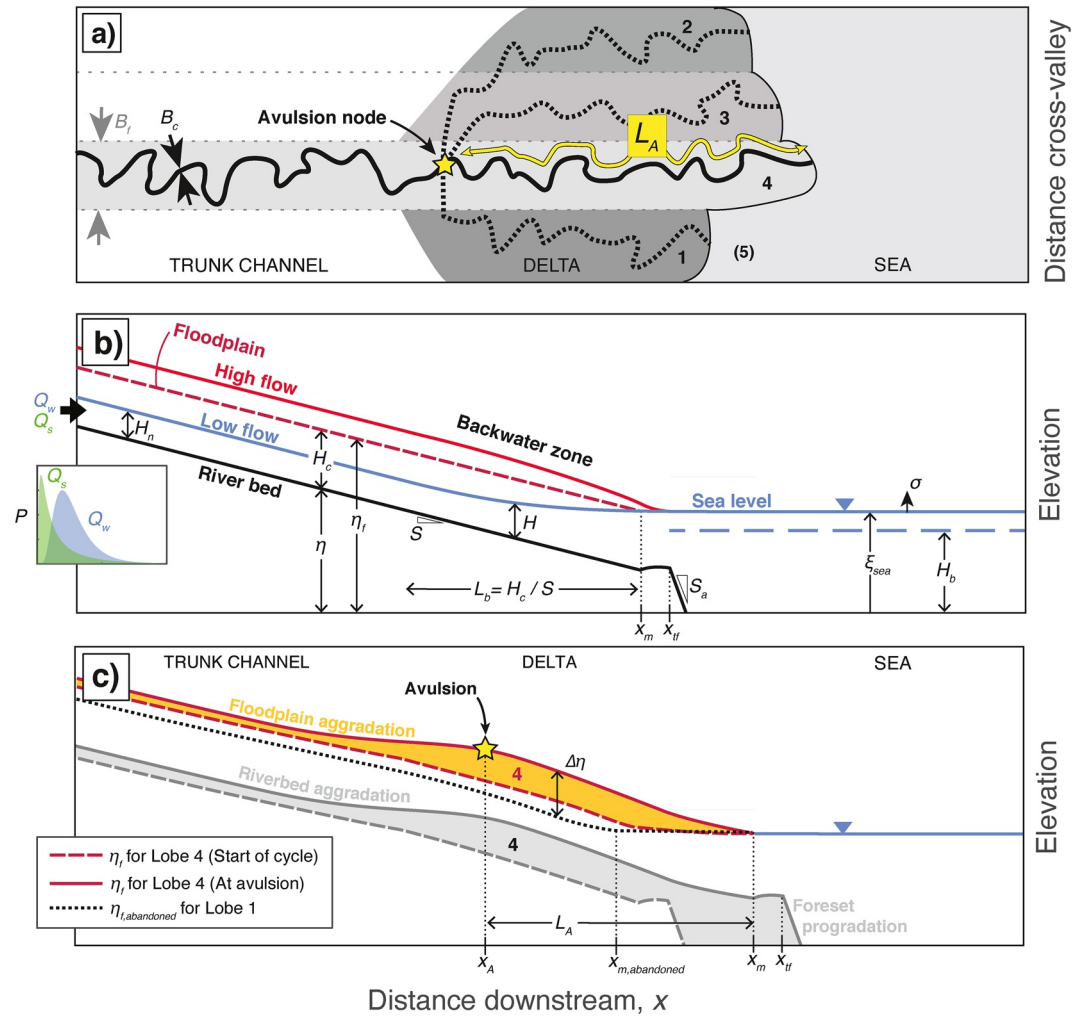


Figure 2. (a) Conceptual model in plan view. Black solid lines are active channel of width B_c in a floodplain/lobe of width B_f . Broken lines are abandoned channels. Shaded regions are deposits created during avulsion cycles 1–4. At times of avulsion, the active lobe (in this case, lobe 4) is abandoned and the river is rerouted downstream of the avulsion location (yellow star) to reoccupy the lowest-elevation abandoned lobe (Lobe 1), where it will begin building a new lobe filling in the space indicated by (5). (b) Conceptual model in long profile, showing variable definitions and climate-change boundary conditions of sea-level rise σ , sediment supply Q_s , and flood regime Q_w . (c) Same as (b), but now showing riverbed aggradation and floodplain superelevation ($\Delta\eta$) of the active lobe (Lobe 4) relative to the lowest abandoned lobe (Lobe 1). All delta lobes share a single trunk channel.

2. Model Framework

2.1. Governing Equations

The model is the same as that presented in Chadwick et al. (2019) and is briefly reviewed here. The model is designed to capture the dynamics of repeated delta-lobe construction and avulsion in a simplified, quasi-2D framework. We consider a generic delta plain with an imposed number of lobes that are assumed to form a branching pattern (Figure 2a). Each lobe is modeled as a coupled river and floodplain of constant width (B_f), channel sinuosity (Ω), wash load ratio (Λ), and bed porosity (λ_p) using sediment mass balance (Parker, 2004; Parker et al., 2008),

$$\frac{\partial \eta}{\partial t} = -\frac{(1 + \Lambda)\Omega}{(1 - \lambda_p)B_f} \frac{\partial Q_t}{\partial x} \quad (4)$$

where η is riverbed elevation, t is time, x is downstream distance, and Q_t is the flux of total bed-material load. The river is prescribed an initial topset profile η_0 ending at a foreset at $x = x_{ff}$ (Figure 2b) and Equation 4 is integrated over time using finite differences to determine topset aggradation. Foreset progradation is approximated using a moving boundary formulation, following previous work (Hotchkiss & Parker, 1991; Kostic & Parker, 2003; Swenson et al., 2000), such that all sediment delivered to the foreset contributes to its progradation at a constant slope S_a (Text S1).

At a given time, the river occupies a single lobe where water and sediment are transported in a river channel of prescribed depth (H_c) and width (B_c). Water is routed using a quasi-2D backwater equation for water mass and momentum conservation under quasi-steady flow conditions (Chow, 1959; Sturm & Tuzson, 2001),

$$\frac{dH}{dx} = \frac{S - C_f Fr^2}{1 - Fr^2} + \frac{Fr^2}{1 - Fr^2} \frac{H}{B} \frac{dB}{dx} \quad (5)$$

where H is flow depth, $S = -\frac{\partial \eta}{\partial x}$ is riverbed slope, C_f is friction factor, $Fr = Q_w / (BH\sqrt{gH})$ is Froude number, Q_w is water discharge, g is gravity, and B is flow width. We assume a uniform flow width in the channel, and an offshore plume with a constant spreading angle beyond the river mouth (Chatanantavet et al., 2012; Lamb et al., 2012). The river mouth location (x_m) is set by the intersection of the floodplain profile ($\eta_f = \eta + H_c$) and sea level (ξ_{sea}) (Figure 2b; Text S1) (Chadwick et al., 2019). The river mouth typically occurs slightly upstream of the topset-foreset break in our simulations, allowing for a dynamic water-surface elevation in the zone $x_m < x < x_{ff}$ that is important for reproducing realistic backwater effects during high flows (Text S1) (Chatanantavet et al., 2012; Chatanantavet & Lamb, 2014). Sediment is routed according to the Engelund and Hansen (1967) relation for total bed-material load,

$$Q_t = B\sqrt{RgD^3} \frac{\alpha}{C_f} (\tau^*)^\beta \quad (6)$$

where R is submerged specific gravity of sediment, D is the median grain size of bed material, $\tau^* = C_f(Q_w / BH)^2 / RgD$ is Shields number, $\alpha = 0.05$, and $\beta = 2$.

Climate change affects model behavior through boundary conditions on Equations 4–5. At the downstream boundary, flow depth is determined by sea level,

$$H|_{x=x_{ff}} = \xi_{sea} - \eta|_{x=x_{ff}} \quad (7)$$

where $\xi_{sea} = H_b + \sigma t$ is sea level, H_b is initial basin depth offshore, and σ is the user-specified relative sea-level rise rate (Figure 2b). Far upstream of the backwater zone, the river experiences normal flow conditions $\left(\frac{dH}{dx} = 0\right)$ and Equation 5 reduces to

$$H_n = \left(\frac{C_f Q_w^2}{gSB^2}\right)^{1/3} \quad (8)$$

where H_n is the normal flow depth. Thus, normal flow depth varies according to the flood regime, which is prescribed using a probability distribution P of monthly mean discharges Q_w at the upstream end (Figure 2b) (LeBoutillier & Waylen, 1993; Stedinger, 1993). Sediment supply enters the model domain via a ghost node at the upstream end (Kostic & Parker, 2003) at user-specified time-averaged rate \bar{Q}_s . The instantaneous sediment supply Q_s at the ghost node is covaried with water discharge such that the river maintains transport capacity ($Q_s = Q_t$ in Equation 6) at a constant slope regardless of flow regime, which is a good approximation for lowland rivers downstream of the hydrographic boundary layer (Mackin, 1948; Wong & Parker, 2006),

$$\bar{Q}_s = \int_0^\infty P dQ_s \quad (9)$$

$$Q_s = B\sqrt{RgD^3} \frac{\alpha}{C_f} (H_n S_0 / RD)^\beta \quad (10)$$

where S_0 is the constant slope at the ghost node, obtained by combining and numerically integrating Equations 8–10 for a given flow regime (P, Q_w) and sediment supply (\bar{Q}_s).

Avulsions occur where and when the active lobe first aggrades to a critical height relative to the neighboring lobes (Figure 2c), which is referred to as superelevation ($\Delta\eta$),

$$\Delta\eta(x) \geq H^* H_c \quad (11)$$

where H^* is the avulsion threshold, a dimensionless number of order unity (Ganti, Chadwick, Hassenruck-Gudipati, & Lamb, 2016; Ganti et al., 2014; Mohrig et al., 2000). We measure superelevation as the height of the active lobe floodplain (η_f) relative to the floodplain of the lowest-elevation abandoned lobe ($\eta_{f,abandoned}$), evaluated at the same distance downstream from the trunk channel:

$$\Delta\eta(x) = \begin{cases} \eta_f(x) - \eta_{f,abandoned}(x) & \text{for } x \leq x_{m,abandoned} \\ \eta_f(x) - \xi_{sea} & \text{for } x > x_{m,abandoned} \end{cases} \quad (12)$$

where $x_{m,abandoned}$ is the streamwise coordinate of the abandoned-lobe shoreline (Figure 2c). Seaward of the abandoned lobe, superelevation is measured relative to sea level (ξ_{sea}).

After each avulsion, the river is routed to the lowest abandoned lobe by joining the bed profile of the active channel upstream of the avulsion site with the bed profile of the new flow path downstream,

$$\eta_{new}(x) = \begin{cases} \eta(x) & x \leq x_A \\ \text{MIN}(\eta_{abandoned1}(x), \eta_{abandoned2}(x), \eta_{abandoned3}(x)) & x > x_A \end{cases} \quad (13)$$

where η_{new} is the new riverbed profile after avulsion, η is the riverbed profile before avulsion, x_A is the avulsion location, and $\eta_{abandoned1}$, $\eta_{abandoned2}$, and $\eta_{abandoned3}$ are the three abandoned-lobe long profiles. The MIN operator here selects the abandoned profile that has the minimum mean elevation downstream of the avulsion node. Inactive lobe shapes are unchanged when abandoned (Galloway, 1975) but are partially drowned in cases due to relative sea-level rise. After establishing the new flow path, lobe construction (Equations 4–10) and avulsion setup (Equation 11) begin anew.

2.2. Dimensional Analysis

We non-dimensionalize the model to allow applicability of our results for a broad range of lowland deltas. Equations 4–13 are scaled by a characteristic channel depth (H_c), channel width (B_c), backwater length (L_b), and channel-filling timescale $T_c = \frac{H_c}{\bar{Q}_s / L_b B_f \Omega(1 + \Lambda)}$ (Chatanantavet & Lamb, 2014; Reitz & Jerolmack, 2012) that are assumed constant (Text S2). Dimensional analysis reveals that model behavior is sensitive to six dimensionless input parameters linked to climate change. Delta response to sea-level rise depends on the ratio of rates of sea-level rise and delta aggradation (Chadwick et al., 2020; Ganti et al., 2019; Liang et al., 2016; Muto & Steel, 1997), estimated by the normalized relative sea-level rise rate σ^*

$$\sigma^* = \frac{\sigma}{H_c / nT_c} \quad (14)$$

where $n = (N + 1) / 2$ is a constant representing the average number of avulsions before a given lobe is reoccupied (Ganti et al., 2019) and N is the imposed number of delta lobes (Figure 2a). The denominator of Equation 14 represents a first-order estimate of the maximum possible aggradation rate, i.e., the delta's capacity to aggrade in the face of sea-level rise, assuming all sediment is deposited uniformly across the

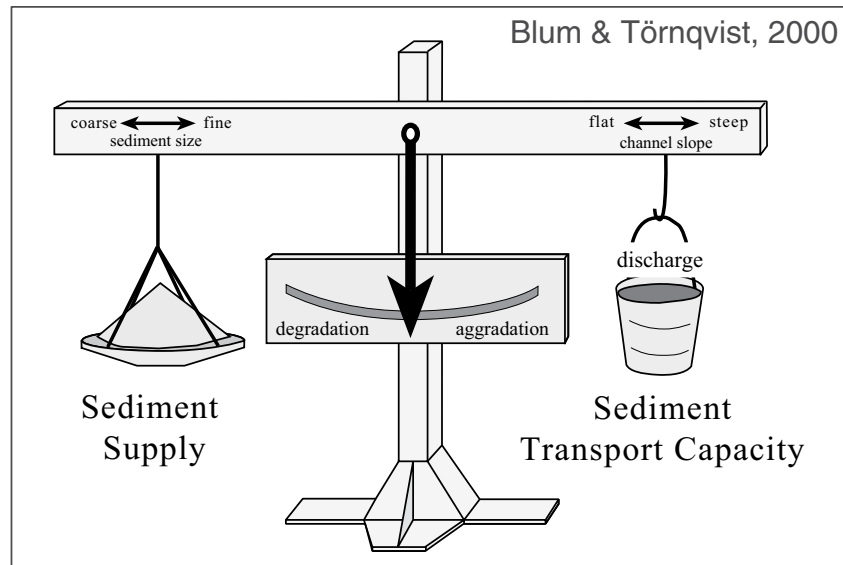


Figure 3. Conceptualization of balance between sediment supply and transport capacity, redrawn by Blum and Törnqvist (2000) from an unpublished schematic by W. Borland and based on an equation from Lane (1955). Decreasing water discharge, increasing sediment supply, and/or increasing sediment size causes sediment supply to exceed capacity, resulting in aggradation. Conversely, increasing water discharge, decreasing sediment supply, and/or decreasing sediment size causes sediment transport capacity to exceed sediment supply, resulting in degradation.

backwater-scaled topset (Chadwick et al., 2020). When $0 < \sigma^* \lesssim 1$, sea level rises slowly compared to the maximum aggradation rate, and deltas are expected to keep pace with sea level—at least until undergoing autoretreat (Muto et al., 2007). In contrast, when $\sigma^* \gtrsim 1$, sea level rises quickly compared to the maximum possible aggradation rate, and deltas are expected to drown.

Under changing water and sediment supply, fluvial response depends on the imbalance between sediment supply and the sediment transport capacity (Howard, 1982; Schumm, 1993) (Figure 3). We describe this imbalance in terms of the fractional difference between the sediment supply and transport capacity, δQ_s , given by

$$\delta Q_s = \frac{\bar{Q}_s - \bar{Q}_{t0}}{\bar{Q}_{t0}} \quad (15)$$

where \bar{Q}_{t0} is the initial sediment transport capacity, time-averaged over the normal flow regime using Equations 6 and 8. Sediment transport capacity describes the amount of sediment the channel is able to transport, and is generally greater for rivers with higher water discharges, steeper slopes, and finer sediment. When $\delta Q_s > 0$, sediment supply exceeds the river's transport capacity, and the riverbed is expected to steepen its slope via a downstream-propagating wave of aggradation (Schumm, 1993). In contrast, when $\delta Q_s < 0$, sediment supply is less than the sediment transport capacity of the river, and the riverbed is expected to decrease its slope through a downstream-propagating wave of incision. In either case, slope adjustment over time changes the river's transport capacity (Equation 6) until it matches the sediment supply and $\delta Q_s = 0$. When $\delta Q_s = 0$, sediment supply and transport capacity are in balance, and the riverbed is expected to maintain a constant slope (Mackin, 1948), at least for a case without river mouth progradation (Bijkerk et al., 2016). Sediment supply and sediment transport capacity are both non-negative quantities, and so δQ_s is always greater than -1 .

The flood regime is described by a log-normal distribution of monthly mean discharges (LeBoutillier & Waylen, 1993; Stedinger, 1993), which is uniquely defined in terms of a bankfull exceedance probability F_{bf} and coefficient of variation of stage height CV (Chadwick et al., 2019) (Figure S1). The bankfull exceedance probability F_{bf} describes the frequency of overbank flows ($H_n > H_c$) relative to all possible flows, and can range from 0 to 1. The coefficient of variation CV describes the magnitude of low flows and high flows

relative to the average flow, and is defined by the standard deviation of the normal flow depth divided by the mean. Another important aspect of flood regimes is the duration of individual flood events, relative to the timescales of bed aggradation in the backwater zone (Chatanantavet & Lamb, 2014), which we describe in terms of the normalized flood event duration T_e^* ,

$$T_e^* = \frac{T_e}{T_c} \quad (16)$$

where T_e is the prescribed duration of individual flood events. When $T_e^* \ll 1$, as is the case for many rivers, individual floods are too short to cause significant bed aggradation, allowing for a state of perpetual riverbed adjustment in the backwater zone and, as a result, persistent backwater hydrodynamics (Chatanantavet & Lamb, 2014). When $T_e^* \gtrsim 1$, in contrast, floods are long enough to fully adjust the backwater reach to normal flow conditions, and so backwater effects are muted. Previous work suggests flood regimes can also affect the amount of aggradation necessary to trigger an avulsion (Ganti et al., 2014), which we describe in terms of the avulsion threshold H^* in Equation 11. The avulsion threshold varies between 0.2 and 1.1 on lowland deltas, with lower avulsion thresholds generally associated with higher CV (Ganti et al., 2014).

In addition to the six climate-change parameters (σ^* , δQ_s , F_{bf} , CV , T_e^* , H^*), there are an additional six model input parameters that need to be specified related to delta geometry, flow hydraulics, and sediment transport. These are: the offshore basin depth (H_b) relative to the channel depth, the lobe width (B_f) relative to the channel width, the number of delta lobes (N), the bankfull Froude number in the normal flow reach ($Fr_{n,bf}$), the bankfull Shields number in the normal flow reach ($\tau_{n,bf}^*$), and the friction factor (C_f).

Results for avulsion location and frequency are also cast in terms of normalized quantities. The normalized avulsion length $L_A^* = \frac{L_A}{L_b}$ describes the ratio of the avulsion length to the backwater length-scale (Equation 3). The normalized avulsion frequency $f_A^* = \frac{f_A}{1/T_c}$ describes the ratio of the avulsion frequency to the characteristic frequency the river aggrades to a height of one channel depth, $1/T_c$ (Equation 1) Both L_A^* and f_A^* are expected to be of order unity for backwater-scaled deltas (Figures 1c and 1e).

3. Model Implementation

To compare avulsion location and frequency on deltas under different climate-change scenarios, we systematically vary parameters related to changing sea level, sediment supply and transport capacity, and flood regime (σ^* , δQ_s , F_{bf} , CV , T_e^* , H^*) (Table 1; Text S3). These parameters are specified for simplicity because their connection to global radiation balance and atmospheric and oceanic circulation is site-specific and scale-dependent (Blum & Törnqvist, 2000; Knox & Wright, 1983; Langbein & Schumm, 1958). Model governing equations (Equations 4–13) are non-dimensionalized and solved using finite-difference methods (Text S2–S3). Each model delta is run for nine consecutive avulsion cycles, an arbitrary but reasonable number based on available field data (Table 1). For each avulsion cycle, we measure the avulsion length L_A as the stream-wise distance between the avulsion location (x_A) and the mouth of the parent channel (x_m) (Figure 2c). We measure the time between avulsions T_A and calculate the avulsion frequency using $f_A \equiv 1/T_A$.

At the start of each model run, the initial alluvial plain is assumed planar with a uniform downstream slope set to the transport slope for normal flow (S_0), similar to previous studies (Figure 2b) (Chatanantavet et al., 2012; Moran et al., 2017; Ratliff et al., 2018). The alluvial plain begins at $x = 0$ and ends with an initial foreset at $x_{if} = 6L_b$ (Chatanantavet et al., 2012; Lamb et al., 2012). The transition from the trunk channel to the delta within the alluvial plain is not prescribed and instead emerges naturally from the model based on the location of preferential avulsion (Figure 2a). Each model run begins with a spin-up phase during which the river occupies each lobe at least once; the spin-up phase was found to be necessary to produce avulsions with locations that were not influenced by the initial conditions (Chadwick et al., 2019). By the end of the spin-up period, the topset aggrades to a quasi-steady slope profile (Arkesteijn et al., 2019; Bijkerk et al., 2016) and the foreset progrades to $x_{if} \cong 6.5L_b$. Here we

Table 1
Model Runs and Natural Deltas

Model runs	Climate parameters						Additional parameters						Number of avulsions
	σ^*	δQ_s	CV	F_{bf}	T_e^*	H^*	$\frac{H_b}{H_c}$	$\frac{B_f}{B_c}$	N	$Fr_{n,bf}$	$\tau_{n,bf}^*$	C_f	
	[-]	[-]	[-]	[-]	[-]	[-]	[-]	[-]	[-]	[-]	[-]	[-]	
Base-case climate scenario	0	0	0.53	0.05	1.0E-03	0.5	2	40	4	0.18	1	0.005	9
Sea-level change runs	-1 to 5	0	0.53	0.05	1.0E-03	0.5	2	40	4	0.18	1	0.005	9
Sediment supply & transport capacity runs	0	-0.75 to 1.33	0.53	0.05	1.0E-03	0.5	2	40	4	0.18	1	0.005	9
Coefficient of variation runs	0	0	0 to 0.85	0.05	1.0E-03	0.5	2	40	4	0.18	1	0.005	9
Bankfull exceedance probability runs	0	0	0.53	0.01 to 0.2	1.0E-03	0.5	2	40	4	0.18	1	0.005	9
Flood-event duration runs	0	0	0.53	0.05	1.0E-06 to 1.0E-01	0.5	2	40	4	0.18	1	0.005	9
Avulsion threshold runs	0	0	0.53	0.05	1.0E-03	0.2 to 2	2	40	4	0.18	1	0.005	9
Natural deltas													
Parana	2.3	-	0.18	0.12	1.9E-04	0.69	3.4	-	-	0.09	0.98	0.005	-
Danube	0.076	-	0.27	0.10	3.0E-03	0.79	7.9	-	-	0.10	0.66	0.005	5
Nile	3.7	-	0.65	0.05	6.4E-02	-	7.4	-	-	0.11	1.62	0.005	-
Mississippi	0.29	-	0.44	0.06	1.8E-03	0.60	3.8	-	-	0.09	1.88	0.005	6
Assiniboine	-	-	-	-	2.8E-03	0.33	1.7	-	-	0.32	2.63	0.005	-
Rhine-Meuse	2.6	-	-	-	2.0E-04	0.46	3.6	-	-	0.15	0.69	0.005	22
Magdalena	0.15	-	-	-	5.5E-03	-	33.3	-	-	0.14	1.02	0.005	-
Orinoco	0.77	-	0.61	0.43	7.4E-04	0.26	13.8	-	-	0.11	1.00	0.005	-
Mid-Amazon	0.47	-	-	-	8.7E-04	-	4.2	-	-	0.08	0.90	0.005	-
Upper Rhone	1.0	-	-	-	6.4E-04	0.54	12.9	-	-	0.09	0.61	0.005	6
Yellow	0.0043	-	0.91	0.22	3.8E-01	0.20	8.6	-	-	0.14	2.19	0.005	10
Brahmaputra	0.80	-	0.68	0.08	3.7E-03	1.43	11.4	-	-	0.14	0.88	0.005	7
Goose	-0.13	-	-	-	2.0E-02	0.33	5.0	-	-	0.68	8.46	0.005	4
Mitchell	-0.033	-	-	-	1.9E-03	-	2.1	-	-	0.24	-	0.005	-
Trinity	0.69	-	-	-	2.1E-03	-	1.6	-	-	0.18	2.00	0.005	-

Note. Natural delta values were calculated in Chadwick et al (2020) using field data reported in previous work (Bintanja et al, 2005; Chatanantavet et al., 2012; Ericson et al, 2006; Ganti et al, 2014; Giosan et al, 2006; Jelgersma, 1996; Jerolmack & Mohrig, 2007; T. I. Lane et al, 2017; Milliman et al, 1989; Milliman & Syvitski, 1992; Moran et al, 2017; Nijhuis et al, 2015; Syvitski, 2008; Syvitski & Saito, 2007; Törnqvist et al, 2008; Yu et al, 2012). For natural deltas, normalized rise rates (σ^*) correspond to the late Holocene, with the exception of the Huanghe where pre-industrial historical avulsions are recorded (Ganti et al, 2014).

present results for avulsions after the spin-up period. Climate variables (σ^* , δQ_s , F_{bf} , CV , T_e^* , H^*) are not changed until the end of the spin-up period (Text S3).

4. Results

4.1. Avulsions in a Base-Case Climate Scenario

To provide reference for the climate-change scenarios, we first consider a model run under a base-case climate scenario. The base case corresponds to a constant sea level ($\sigma^* = 0$), balanced sediment supply and capacity at the upstream end ($\delta Q_s = 0$), and a moderate flood regime which is necessary for realistic backwater-scaled avulsion nodes in the model ($CV = 0.53$, $F_{bf} = 0.05$, $T_e^* = 0.001$) (Table 1) (Chadwick et al., 2019;

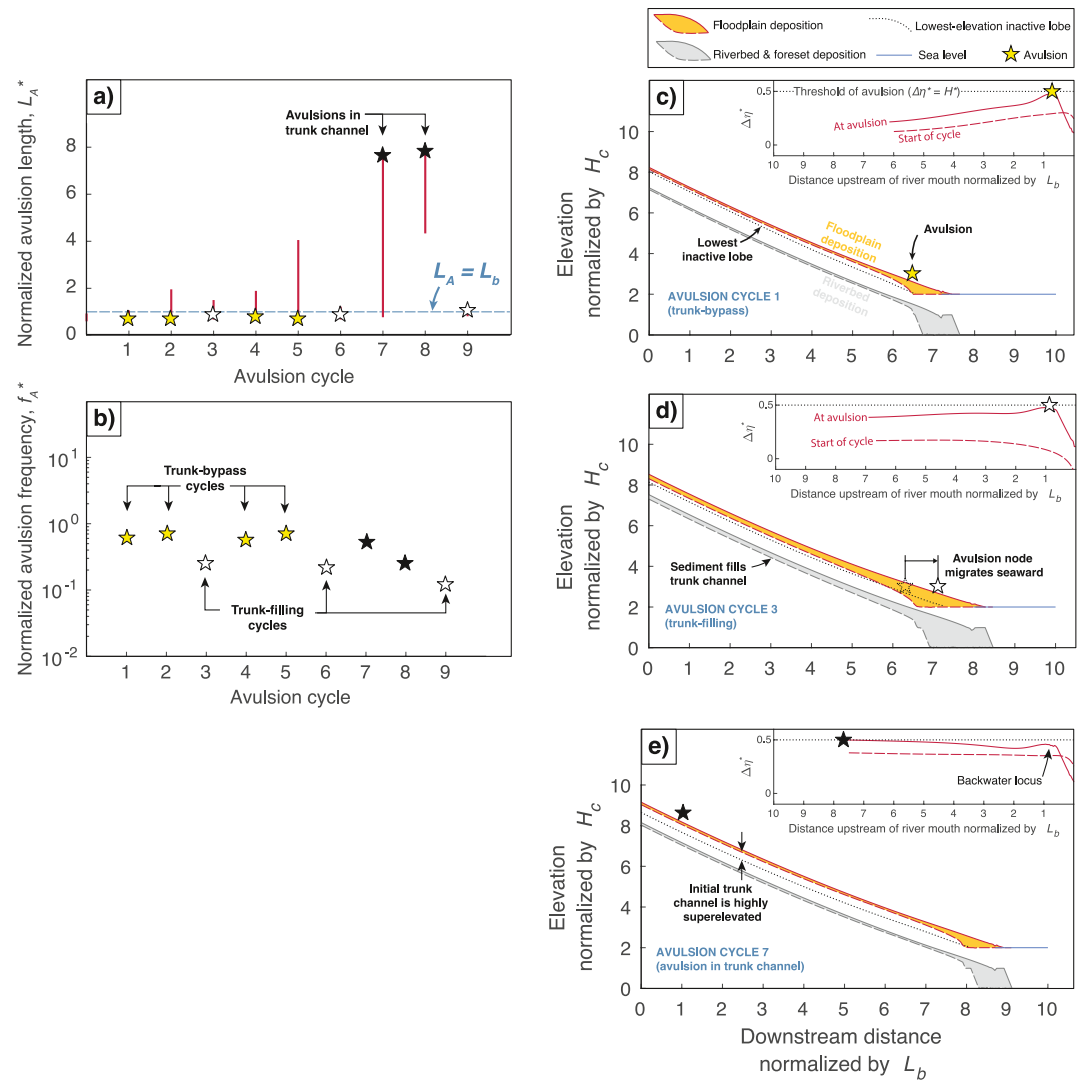


Figure 4. Model results for the base-case climate scenario. (a) Normalized avulsion length and (b) normalized avulsion frequency over nine consecutive avulsion cycles. Trunk-bypass avulsion cycles, trunk-filling avulsion cycles, and avulsions in the trunk channel are colored yellow, white, and black, respectively. Red error bars in (a) indicate the length of river reach within 5% of the avulsion threshold at time of avulsion, and blue dashed line corresponds to an avulsion length equal to the backwater length-scale ($L_A = L_b$). (c–e) Long-profile evolution during avulsion cycles 1, 3, and 7. Shaded regions show deposition on the riverbed and foreset (gray) and on the floodplain (orange) over one avulsion cycle. Floodplain profiles of the active lobe (red lines, shown for the start and end of the avulsion cycle) and the lowest inactive lobe (black dotted line) are used to calculate superlevation (see inset). Stars show avulsion location.

Chatanantavet et al., 2012; Ganti, Chadwick, Hassenruck-Gudipati, Fuller, et al., 2016). Avulsions are triggered when the active lobe aggrades to a height of 50% the channel depth above neighboring abandoned lobes (i.e., $H^* = 0.5$). We adopt constant values for other parameters (H_b , B_f , N , $Fr_{n,bf}$, $\tau_{n,bf}^*$, C_f) which are representative of lowland deltas (Table 1) and correspond to a delta that builds onto a continental shelf with an initial offshore depth twice that of the channel ($H_b = 2H_c$), and a channel with a bankfull Froude number of $Fr_{n,bf} = 0.17$, bankfull Shields number of $\tau_{n,bf}^* = 1$, and friction factor of $C_f = 0.005$. We assume all deltas are composed of four lobes ($N = 4$) with a width of 40 times the channel width ($B_f = 40B_c$), which are reasonable estimates (Coleman et al., 1998; Hayden et al., 2019; Pang & Si, 1979; Parker et al., 2008).

A preferential avulsion length emerges in the model and scales with the backwater length-scale (Figure 4a). In seven of nine avulsion cycles, avulsion length is approximately equal to the backwater length-scale ($L_A^* = L_A/L_b \sim 1$) and only a short reach ($< 0.5L_b$) is within 5% of the avulsion threshold at times of

avulsion. The preferential avulsion length originates from flood variability in the backwater zone (Chadwick et al., 2019; Chatanantavet et al., 2012; Ganti, Chadwick, Hassenruck-Gudipati, Fuller, et al., 2016). Low flows enhance deposition in the backwater zone, and high flows intermittently scour the bed near the river mouth, resulting in a spatial peak in net aggradation rate midway through the backwater zone, termed the locus of deposition (Chatanantavet et al., 2012). Avulsions occur at the locus of deposition, because superelevation is maximized there (Figure 4c). Normalized avulsion frequency is of order unity ($f_A^* \cong 0.1 - 1$), with a median of $f_A^* = 0.55$ (Figure 4b).

Despite constant sea level, sediment supply, and flood regime, we observe inherent variability in avulsion location and frequency due to intermittent filling of the trunk channel upstream of the avulsion node. During most avulsion cycles (cycles 1, 2, 4, 5), sediment is deposited primarily downstream of the avulsion node, and the active lobe grows to a thickness of $\sim H^*H_c$ before an avulsion occurs (Figure 4c). We term these events trunk-bypass avulsion cycles, due to their tendency to maintain sediment bypass conditions within the trunk channel, upstream of the avulsions. In contrast, some cycles (cycles 3, 6, 9) feature trunk channel aggradation to a thickness of $\sim H^*H_c$, and the active lobe grows twice as thick ($\sim 2H^*H_c$) (Figure 4d). We term these trunk-filling avulsion cycles. Avulsion frequency is reduced during trunk-filling avulsion cycles ($f_A^* = 0.26, 0.21, 0.22$ for cycles 3, 6, and 9 respectively) compared to the median ($f_A^* = 0.55$) (Figure 4b). Trunk-filling avulsion cycles also feature greater distances of foreset progradation (Figure 4d) compared to trunk-bypass avulsion cycles (Figure 4c), leading to downstream translation of the avulsion node with a constant avulsion length.

Trunk-filling avulsion cycles occur at every third avulsion cycle because that is when the delta has aggraded all but one of its four lobes. Aggradation of the final lobe by $\sim H^*H_c$ is insufficient to cause an avulsion, because superelevation is still approximately zero compared to abandoned lobes. Instead, the river continues to aggrade until the active lobe reaches a thickness of $\sim 2H^*H_c$, at which point the avulsion node is super-elevated by H^*H_c relative to abandoned lobes, triggering an avulsion. The larger depositional thickness of the lobe requires more time to aggrade, resulting in reduced avulsion frequency. Because these avulsions are less frequent, the active lobe also experiences prolonged progradation, and, as the river system lengthens, the trunk channel fills with sediment to maintain a constant transport slope (Figure 4d) (Ganti et al., 2014; Mackin, 1948). Thus, our model results are consistent with the conceptual model of Ganti et al. (2019) where, for a prograding delta, there are a series of avulsions at a relatively fixed node, followed by less frequent node-shifting avulsions that move the avulsion node seaward in concert with trunk channel aggradation and overall delta progradation.

While both the trunk-filling and trunk-bypass avulsions occur within the backwater zone, during avulsion cycles 7 and 8, avulsions occur far upstream of the backwater zone ($L_A^* \gg 1$). For these upstream avulsions, an extensive river reach ($> 2L_b$) is within 5% of the avulsion threshold (Figure 4a), indicating that avulsion occurrence has a similar likelihood throughout the trunk channel. These upstream avulsions occur because the trunk aggraded substantially during the previous trunk-filling cycle, cycle 6, leaving the trunk channel highly superelevated relative to inactive lobes (Figure 4e). The river maintains near sediment-bypass conditions in the trunk channel during cycles 7 and 8, but in this case minor aggradation (associated with progradation) is sufficient to trigger an avulsion in the trunk channel before the depositional locus in the backwater zone becomes fully superelevated (Figure 4e inset). With the next phase of trunk channel aggradation in cycle 9, avulsions resume in the backwater zone (Figure 4a).

4.2. Effects of Sea-Level Change on Avulsion Location and Frequency

For this set of model runs, we systematically vary the normalized sea-level rise rate from $-1 < \sigma^* < 5$, which covers the range of eustatic sea-level swings during the Holocene (Bintanja et al., 2005; Ganti et al., 2019) (Table 1). For simplicity, we adopt a constant rate of sea-level rise or fall for each model run. These model runs feature a steady sediment supply ($\delta Q_s = 0$), a moderate flood regime ($CV = 0.53, F_{bf} = 0.05, T_e^* = 0.001, H^* = 0.5$) identical to the base-case climate scenario, and other parameters are also equivalent to the base case ($H_b = 2H_c, B_f = 40B_e, N = 4, Fr_{n,bf} = 0.17, \tau_{n,bf}^* = 1, C_f = 0.005$).

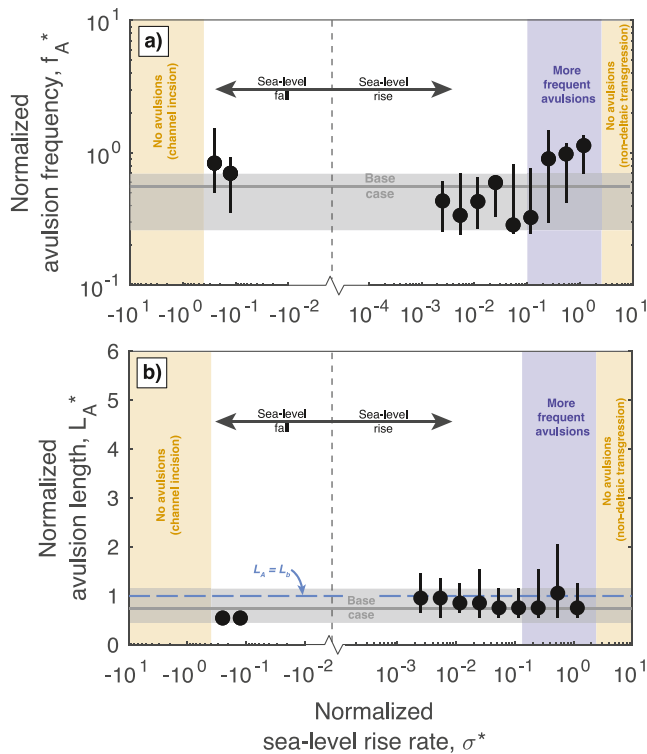


Figure 5. (a) Model results for normalized avulsion frequency f_A^* (a) and normalized avulsion length L_A^* (b) under changing normalized sea-level rise rate σ^* . Black circles are the median avulsion location and frequency over 9 avulsion cycles. Black error bars show autogenic variability in avulsion frequency and length over the same 9 cycles, corresponding to the 25–75 percentile range of avulsion frequency in (a) and the average reach within 5% of the avulsion threshold at times of avulsion in (b). Median and autogenic variability for the base case are indicated by the gray line and shaded region, respectively. Blue shaded region highlights conditions where sea-level rise causes more frequent avulsions, and orange shaded regions highlight conditions where no avulsions occurred due to non-deltaic transgression (Tomer et al., 2011) or incision of the channel.

Consistent with the results shown in Chadwick et al. (2020), avulsion frequency increases with increasing sea-level rise rate in the range $0.1 < \sigma^* < 1$ (Figure 5a). Under these conditions, the relative sea-level rise rate is similar to the maximum possible delta aggradation rate, and the river responds to increasing sea-level rise rate by partitioning more of the sediment load to topset aggradation relative to foreset progradation. For $\sigma^* < 0.1$, sea-level change is too slow to affect avulsion frequency (Figure 5a). Instead, the rate of topset aggradation and avulsion is set by the pace of foreset progradation, consistent with previous work (Moodie et al., 2019; Ratliff et al., 2018). Avulsions are also more frequent during sea-level fall ($\sigma^* < 0$) than during the base case with constant sea level (Figure 5a) because progradation rate increases over time as the offshore basin shallows, consistent with observations of natural and experimental deltas (Bijkerk et al., 2016; Carlson et al., 2018; T. I. Lane et al., 2017; Nijhuis et al., 2015). Avulsions do not occur when $\sigma^* < -0.4$ because sea-level fall causes channel incision, nor when $\sigma^* > 2.5$ because sea level rises to drown the entire model domain before the channel is sufficiently superelevated (Figure 5). In the latter case, no sediment is delivered to the river mouth and the system may be classified as non-deltaic (Tomer et al., 2011). In all model runs, we observe variability in avulsion location and frequency (see error bars on Figure 5) that originates from intermittent filling of the trunk channel upstream of the avulsion node, similar to the base-case scenario (Figure 4). Across all sea-level change runs, trunk-bypass avulsion cycles compose the majority of avulsions (55%). Similar to the base case, trunk-filling avulsion cycles occur every 3 avulsion cycles, comprising 33% of all avulsions. Avulsions in the trunk channel are relatively rare (12%) and, like the base case, occur when the trunk channel is left highly superelevated after a trunk-filling avulsion cycle.

Regardless of sea-level change, avulsion lengths remain approximately constant and equal to the backwater length-scale ($L_A^* = L_A / L_b \sim 1$) (Figure 5b). The backwater-scaled avulsion length originates from variable-discharge flows that produce a spatial maximum in aggradation rate midway through the backwater zone, similar to the base case. Median avulsion length decreases slightly as rise rate increases, but the reduction is negligible compared to the range of autogenic variability (Figure 5b).

Because avulsion length remains constant, the avulsion node migrates seaward and landward in tandem with the shoreline. For example, under constant sea level, the avulsion node migrates downstream as the delta shoreline progrades seaward (Figures 6a and 6b), similar to observations of natural and laboratory deltas (Ganti, Chadwick, Hassenruck-Gudipati, Fuller, et al., 2016; Ganti et al., 2014). Sea-level rise reduces the rate of progradation, stabilizing both the shoreline and the avulsion node (Figures 6c and 6d). When sea level rises fast enough to outpace delta-top aggradation, the shoreline retreats landward, and the avulsion node migrates upstream in tandem (Figures 6e and 6f). Depending on the rise rate, the trunk channel extends or shortens such that the entire river system (delta and trunk channel) approaches a length of L_{auto} (Figures 6c and 6e) (Equation 2) (cf., Muto et al., 2007). However, the size of the delta itself—the region of subaerial land downstream of the avulsion node—remains approximately constant and set by L_b due to backwater effects (Equation 3).

Cases with $\sigma^* \ll 1$ are similar to the base-case scenario in that the avulsion node shifts downstream every three avulsion cycles during a phase of trunk-channel filling (Figures 6a and 6c). In contrast, when $\sigma^* \gtrsim 1$, the avulsion node migrates upstream during every avulsion cycle, not only during trunk-filling cycles, because sea-level rise forces the river mouth and backwater zone farther landward each time a lobe

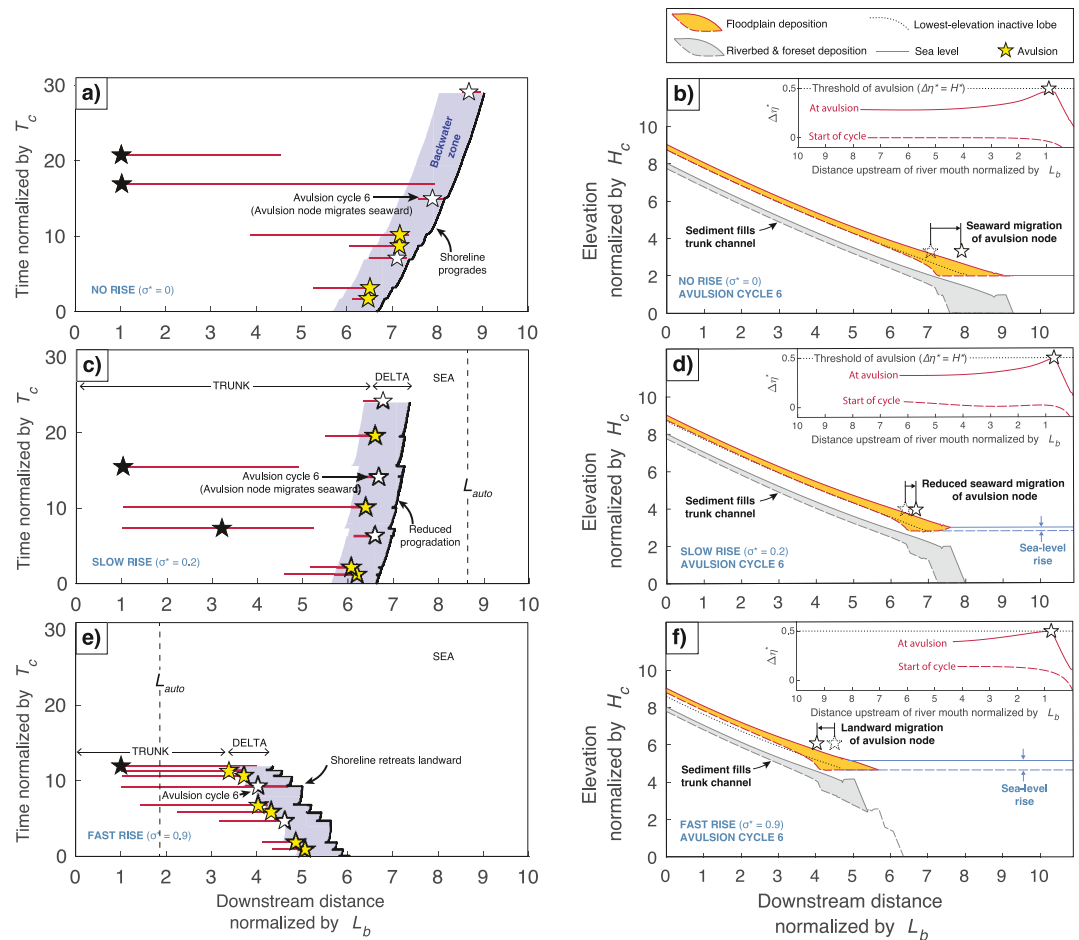


Figure 6. (a) Shoreline trajectory and avulsion node migration for constant sea level. Black line is the shoreline and stars are avulsions. Trunk-bypass avulsion cycles, trunk-filling avulsion cycles, and avulsions in the trunk channel are colored yellow, white, and black, respectively. Red error bars indicate the reach within 5% of the avulsion threshold at times of avulsion, and blue shaded area indicates the backwater zone. (b) Example of trunk-filling avulsion cycles and associated migration of the avulsion node for constant sea level. (c–d) Same as (a–b), but for slow sea-level rise. (e–f) Same as (a–b), but for rapid sea-level rise. Vertical dashed lines in (c) and (e) show autostratigraphic length-scale L_{auto} (Equation 3), and in (a) $L_{auto} \rightarrow \infty$.

is reoccupied (Figure 6e). Reoccupied lobes prograde a thin foreset wedge atop the drowned delta plain, creating a series of back-stepping lobe deposits (Figure 6f).

4.3. Effects of Sediment Supply on Avulsion Location and Frequency

For these model runs, sediment supply is varied from 25% to 233% of the sediment transport capacity ($\delta Q_s = -0.75$ to 1.33). For simplicity, we implement instantaneous step-wise changes in the sediment supply at the start of each model run. Exploring more gradual changes could be done in the future; the step-wise changes are a starting point to understand model sensitivity, and delta response to more gradual changes can be inferred from model runs with small instantaneous changes in δQ_s to the extent that long-term change can be approximated by a series of small step-wise changes. Model inputs are otherwise identical to that of the base-case climate scenario, featuring steady sea level ($\sigma^* = 0$) and a moderate flood regime ($CV = 0.53, F_{bf} = 0.05, T_e^* = 0.0001$). Minor changes in CV and F_{bf} are incurred when the transport slope adjusts to the new sediment supply because the relationship between water discharge and flow depth depends on slope (Equation 8), but we find this effect is negligible in our model runs. Other model parameters are held constant at base-case conditions ($H_b = 2H_c, B_f = 40B_c, N = 4, Fr_{n,bf} = 0.17, \tau_{n,bf}^* = 1, C_f = 0.005$).

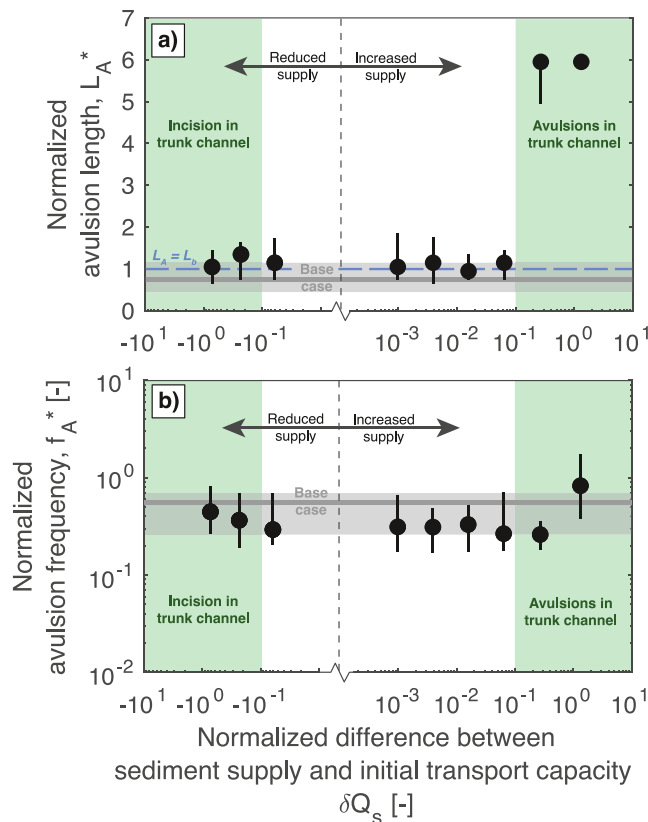


Figure 7. Model results for normalized avulsion length L_A^* (a) and normalized avulsion frequency f_A^* (b) with changes to the normalized difference between sediment supply and initial transport capacity δQ_s . Black circles are the median avulsion location and frequency over 9 avulsion cycles. Black error bars show autogenic variability in avulsion length and frequency over the same 9 cycles, corresponding to the average reach within 5% of the avulsion threshold at times of avulsion in (a), and the 25–75 percentile range of avulsion frequency in (b). Median and autogenic variability for the base case are indicated by the gray line and shaded region, respectively. Green shaded regions highlight conditions where reduced sediment supply caused incision in the trunk channel ($\delta Q_s < -0.1$), and where increased sediment supply caused avulsions in the trunk channel ($\delta Q_s > 0.1$).

Increasing the sediment supply relative to the transport capacity causes aggradation in the trunk channel, which originates from upstream and propagates downstream, as expected (Blum & Törnqvist, 2000; Howard, 1982; Mackin, 1948; Schumm, 1993). For $0 < \delta Q_s < 0.1$, the additional upstream sediment supply does not affect avulsion location in the backwater zone, nor does it significantly change the avulsion frequency (Figure 7). However, when sediment supply exceeds 110% of the transport capacity ($\delta Q_s > 0.1$), backwater-scaled avulsions do not occur, and instead avulsions shift to the upstream end of the trunk channel (i.e., at $L_A^* \sim 6$; Figure 7a); because this is the region of the model domain that responds first to sediment supply, it has the highest aggradation rate. Further increases to δQ_s beyond $\delta Q_s = 0.1$ cause more frequent avulsions that also occur at the upstream end of the trunk channel (Figure 7b).

The change in avulsion locations occurs due to a competition between aggradation in the backwater zone, and the downstream-migrating depositional wave in the trunk channel associated with riverbed slope adjustment. For example, when the sediment supply is increased by 6% (Figure 8a), slope adjustment is achieved rapidly—within the first avulsion cycle—with relatively little aggradation. Aggradation in the backwater zone sets the spatial maximum in superelevation, leading to repeated avulsions at $L_A \sim L_b$ (Figure 8b) comparable to the base-case scenario. In contrast, when the sediment supply is increased by 27%, the downstream-migrating depositional wave causes prolonged slope adjustment in the trunk channel that persists over multiple avulsion cycles (Figure 8c). Trunk channel aggradation due to slope adjustment outpaces aggradation in the backwater zone on average, leading to repeated avulsions at the point of maximum aggradation in the upstream end of the trunk channel (Figure 8d). When sediment supply is further increased to 133%, the trunk channel aggrades even more rapidly, causing more frequent avulsions (Figure 8e). In this case, backwater zone aggradation is far less than the rate of trunk channel aggradation, and so little sediment accumulated in the backwater zone between avulsions (Figure 8f). The elapsed time during the nine avulsion cycles is insufficient for the downstream-migrating depositional wave to reach the backwater zone, in part due to the avulsions themselves. Avulsions in the trunk channel interrupt migration of the wave by shifting the zone of sedimentation laterally among lobes (see dashed arrows in Figures 8c and 8e). Over more avulsion cycles than we modeled, we expect that the depositional wave would reach the shoreline and that avulsions would resume in the backwater zone, similar to the base-case scenario.

Model runs with decreased sediment supply relative to the transport capacity ($\delta Q_s < 0$) feature lower aggradation rates in the trunk channel—and in extreme cases, trunk channel incision—which reduce riverbed slopes until the transport capacity matches the sediment supply, consistent with previous work (Blum & Törnqvist, 2000; Howard, 1982; Mackin, 1948; Schumm, 1993). Reducing the sediment supply does not affect avulsion location or frequency, which remain statistically similar to the base case (Figure 7). For example, when the sediment supply is reduced by 6%, slope adjustment is achieved through minor reduction in trunk channel aggradation during the first avulsion cycle (Figure 9a). This minor slope adjustment has little impact on the locus of aggradation and avulsion in the backwater zone (Figure 9b). In another example, a dramatic reduction in sediment supply ($\delta Q_s = -72\%$) causes a downstream-migrating erosional wave in the trunk channel (Figure 9c). The incised trunk channel is entrenched relative to the abandoned floodplain, eliminating avulsions in the trunk channel (Figure 9d). The erosional wave dissipates before reaching the backwater zone; slope adjustment in the backwater zone is achieved instead through delta progradation and aggradation. As a result, aggradation and avulsion in the backwater zone continue uninterrupted.

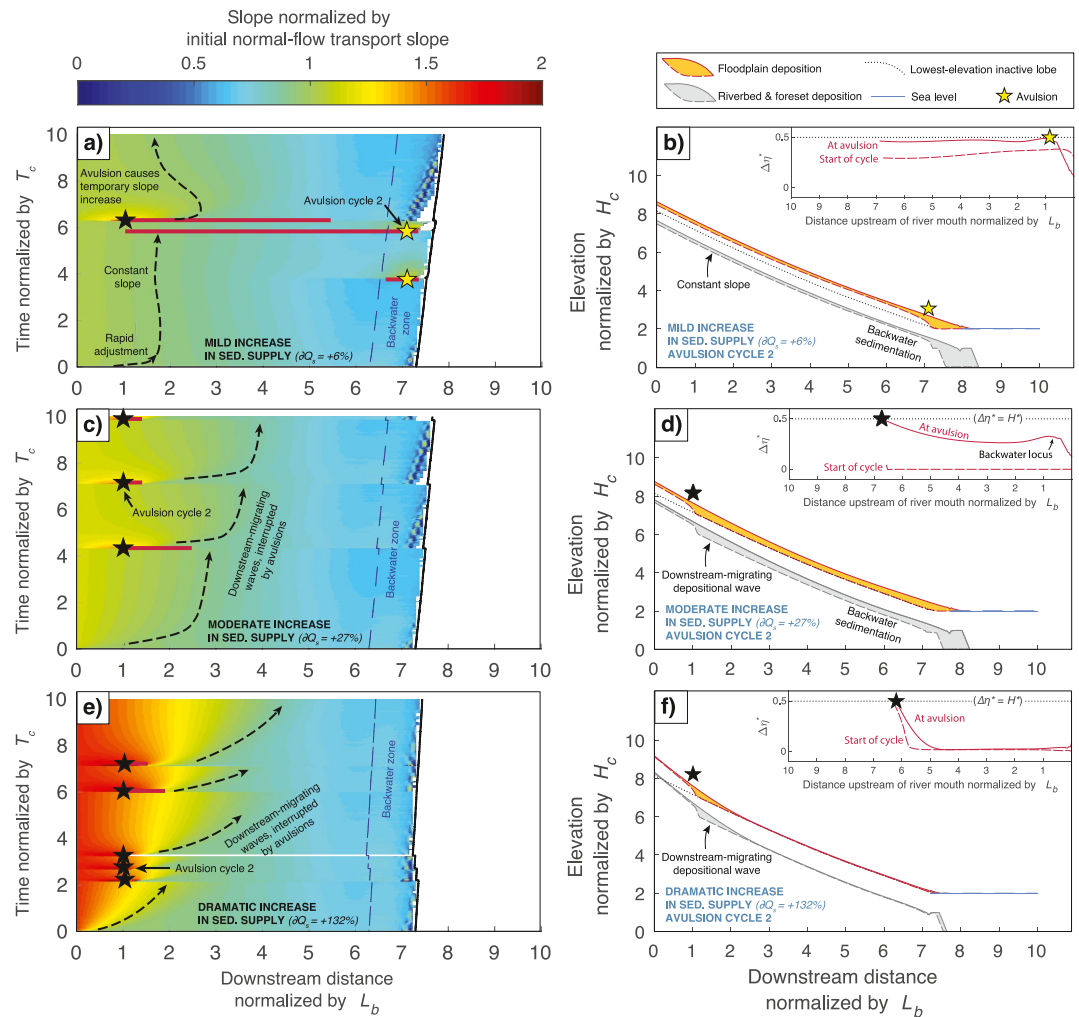


Figure 8. (a) Spatiotemporal trends in riverbed slope during the first 10 normalized time units for mild increase in sediment supply. Warm colors indicate slopes steeper than the initial normal flow transport slope, and cool colors indicate slopes gentler than the initial normal flow transport slope. Dashed black arrows highlight downstream-migrating waves of aggradation, which steepen the topset slope. Black line is the shoreline and stars are avulsions. Trunk-bypass avulsion cycles and avulsions in the trunk channel are colored yellow and black, respectively. Red error bars indicate the reach within 5% of the avulsion threshold at times of avulsion, and blue dashed line indicates where avulsion length is equal to the backwater length-scale. (b) Example of an avulsion cycle for mild increase in sediment supply. (c–d) Same as (a–b), but for moderate increase in sediment supply. (e–f) Same as (a–b), but for dramatic increase in sediment supply.

Regardless of sediment supply changes, the riverbed also experiences temporary increases in channel-bed slope near avulsion locations (Figures 8a, 8c, 8e, 9a and 9c). Slope is increased because river avulsions in our model cause channel steepening and a wave of incision that propagates upstream from the avulsion location, a behavior we observe across all climate scenarios that is consistent with previous work (Ganti et al., 2019). These scours are typically filled rapidly following avulsion, well before the next avulsion occurs.

4.4. Effects of Flood Regime on Avulsion Location and Frequency

In this set of model runs, we systematically change the coefficient of variation of normal-flow depth (CV), the bankfull exceedance probability (F_{bf}), the normalized flood event duration (T_e^*), and the avulsion threshold (H^*) within a reasonable range representative of lowland deltas ($CV = 0.1 - 0.85$, $F_{bf} = 0.01 - 0.20$, $T_e^* = 10^{-6} - 10^{-1}$, $H^* = 0.2 - 2$) (Table 1). For a given model run only a single one of the four flood-regime parameters is varied, with other flood-regime

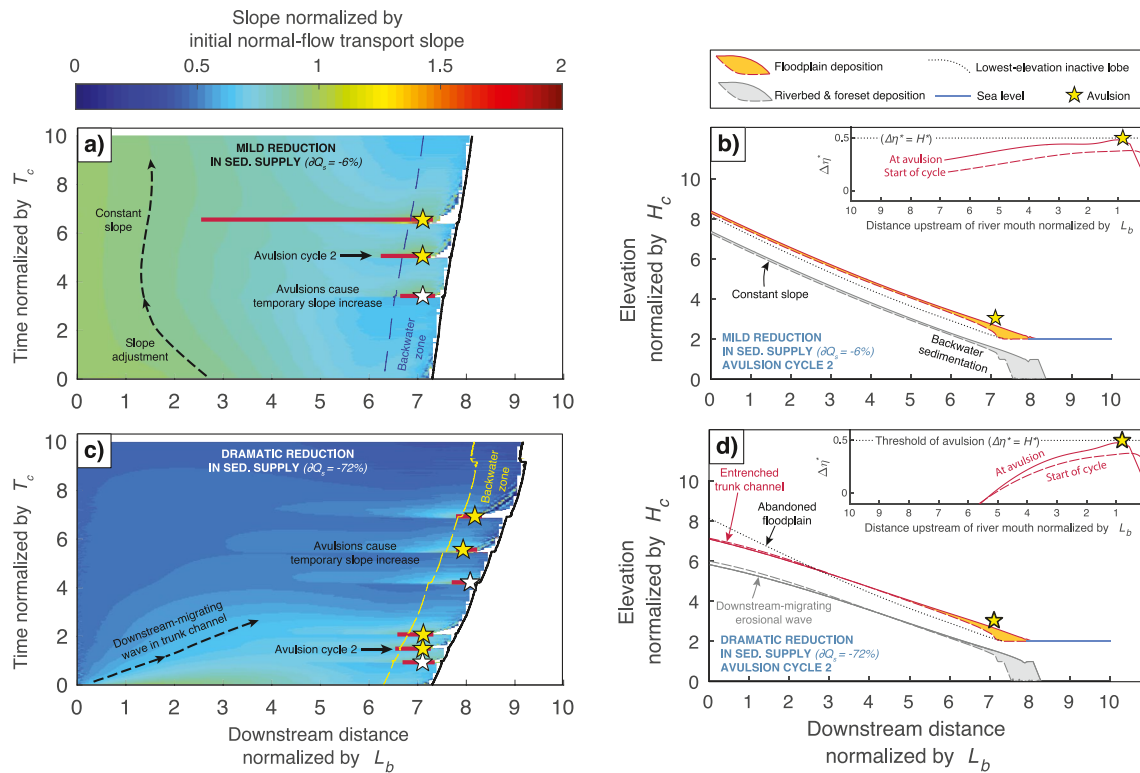


Figure 9. (a) Spatiotemporal trends in topset slope during the first 10 normalized time units for mild reduction in sediment supply. (b) Example of trunk-bypass avulsion cycles for mild reduction in sediment supply. (c–d) Same as (a–b) but for dramatic reduction in sediment supply. Dashed black arrow in (c) highlights downstream-migrating wave of erosion, which reduces the topset slope.

parameters held constant at base-case values ($CV = 0.53, F_{bf} = 0.05, T_e^* = 0.001, H^* = 0.5$). Across all of these runs, sea level is held constant ($\sigma^* = 0$), sediment supply is equal to the transport capacity ($\delta Q_s = 0$), and all other parameters are equivalent to those of the base-case climate scenario ($H_b = 2H_c, B_f = 40B_c, N = 4, Fr_{n,bf} = 0.17, \tau_{n,bf}^* = 1, C_f = 0.005$).

Continuous riverbed adjustment leads to a backwater-scaled avulsion node for coefficients of variation of stage height in the range $0.1 < CV < 0.6$ (Figure 10a), bankfull exceedance probabilities less than 10 percent ($F_{bf} < 0.1$; Figure 10c), and normalized flood durations less than the timescale of channel filling ($T_e^* < 1$; Figure 10e). Under milder flood regimes ($CV < 0.1$) and longer flood durations ($T_e^* > 1$), the riverbed fully adjusts to normal flow conditions, aggradation rate is approximately uniform, and there is no preferential avulsion location (Figures 10a and 10e). Flashier flood regimes ($CV > 0.6$) and higher probabilities of bankfull exceedance ($F_{bf} > 0.1$), also lack a preferential avulsion location (Figures 10a and 10c) because the riverbed adjusts to normal flow conditions associated with large floods. In addition to exploring which conditions produce backwater-scaled avulsions, which also was explored by Chadwick et al. (2019), here we analyze how flood regimes affect avulsion location and frequency.

Changes to flood magnitude (CV) and duration (T_e^*) within the regime of backwater-scaled avulsion nodes has negligible effect on avulsion location or frequency (Figures 10a, 10b, 10e and 10f). However, increasing the flood frequency (F_{bf}) causes avulsions to occur less frequently and farther upstream (Figures 10c and 10d). Flood frequency affects avulsions because floods periodically scour the bed in the backwater zone, reducing long-term aggradation rates. For example, when F_{bf} is increased from 1% to 5%, low-flow deposition is interrupted by frequent floods that scour the backwater reach (Figure 11). Eroded sediment is transported to the river mouth, resulting in enhanced progradation (Figures 11b). Because sediment is frequently repartitioned from the topset to the foreset during large floods, the overall rate of topset aggradation is reduced, and avulsions are less frequent. Furthermore, a greater portion of the backwater zone is within the length of new land on the prograded lobe, seaward of abandoned lobes, where avulsions are unlikely.

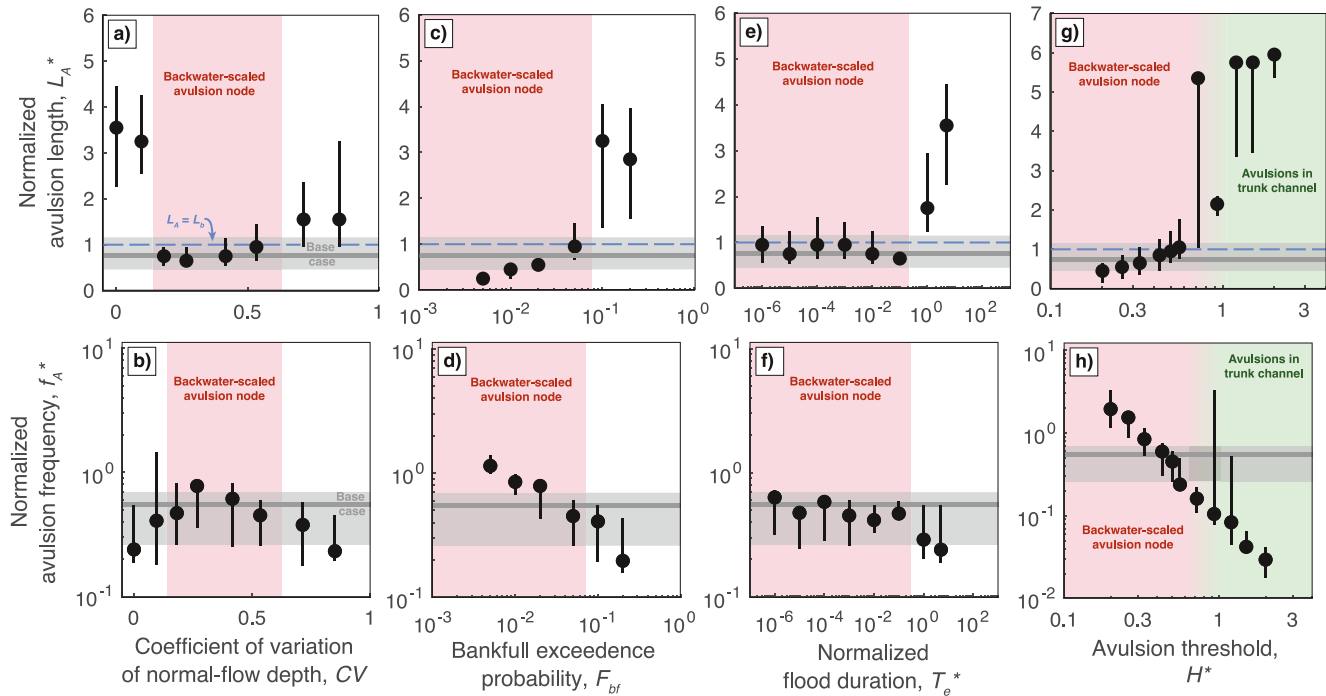


Figure 10. Model results for normalized avulsion length L_A^* and normalized avulsion frequency f_A^* under different flood regimes, including changes to coefficient of variation of normal-flow depth (a–b), bankfull exceedance probability (c–d), normalized flood duration (e–f), and avulsion threshold (g–h). Black circles are median avulsion location and frequency over 9 avulsion cycles. Black error bars show autogenic variability in avulsion length and frequency over the same 9 cycles, corresponding to the average reach within 5% of the avulsion threshold at times of avulsion in (a, c, e, g), and the 25–75 percentile range of avulsion frequency in (b, d, f, h). Median and autogenic variability for the base case are indicated by the gray line and shaded region, respectively. Red shaded regions highlight conditions where flood variability was sufficient to maintain persistent backwater hydrodynamics necessary for a backwater-scaled avulsion node. In (g) and (h), green shaded region highlights conditions where avulsions occurred in the trunk channel because lobes prograded farther than the backwater length-scale over each avulsion cycle, and the gradient between red and green shaded regions highlights the transitional state where only trunk-filling avulsions prograded farther than the backwater length-scale.

Avulsions are unlikely to occur within the length of new land because super-elevation is reduced where it is measured relative to sea level rather than the elevation of abandoned lobes (Equation 12) consistent with previous work (Moodie et al., 2019; Ratliff et al., 2021). As a result, avulsions tend to occur farther upstream, following the maximum in aggradation and super-elevation in the backwater zone (Figures 11b).

Ganti et al. (2014) proposed that the avulsion threshold (H^*) is smaller for rivers with higher CV . To explore this effect, we vary H^* from 0.2 to 2 across model runs. Results show that lower H^* causes more frequent avulsions (Figure 10h) that occur farther downstream (Figure 10g). Avulsions are more frequent because less sediment, and thus less time, is required to aggrade the channel to the avulsion threshold. For example, when $H^* = 0.26$, lobes are thin ($\sim 0.26H_c$) and progradation distances are short ($\sim 0.5L_b$) (Figure 12a). When H^* is increased to 0.5, lobes need to grow thicker ($\sim 0.5H_c$) and prograde farther ($\sim 1L_b$) to reach the greater threshold super-elevation (Figure 12b). Due to the additional time required to build larger lobes, avulsions are less frequent. Increased H^* is also associated with greater avulsion lengths (Figure 10g) because enhanced progradation causes the spatial maximum in super-elevation to shift upstream (Figure 12), similar to model runs with varied F_{bf} (Figure 11).

When the avulsion threshold is increased beyond $H^* > 0.7$, avulsions are less common in the backwater zone and instead shift substantially upstream within the trunk channel (Figure 10g) as a result of enhanced lobe progradation. For instance, when $H^* = 1.5$, the lobe progrades nearly $3L_b$ between avulsions (Figure 12c). For these cases, the amount of lobe progradation is so great that the backwater zone is entirely within the length of the new land on the prograded lobe, seaward of abandoned lobes. As a result, super-elevation is reduced and avulsions are unlikely within the backwater zone (see Figure 12c inset), consistent

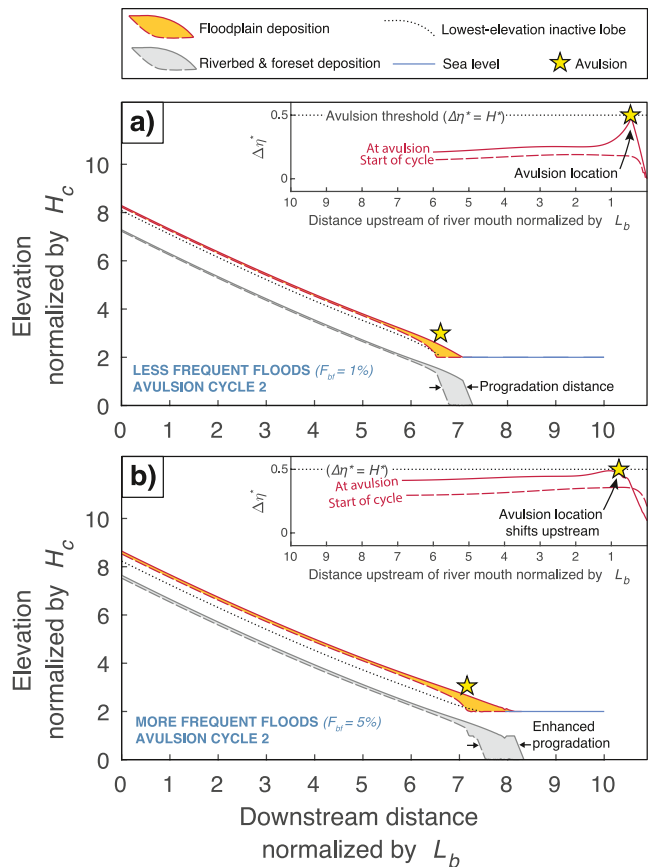


Figure 11. Examples of trunk-bypass avulsion cycles for model runs with less frequent floods (a) and more frequent floods (b). Shaded regions show deposition on the riverbed and foreset (gray) and on the floodplain (orange) over one avulsion cycle. Floodplain profiles of the active lobe (red lines, shown for the start and end of the avulsion cycle) and the lowest inactive lobe (black dotted line) are used to calculate superelevation (see inset). Stars show avulsion location.

the entire river system (delta and trunk channel) approaches L_{auto} through adjustment of the trunk channel length, while the delta maintains a constant size $L_A \sim L_b$ consistent with Equation 3 (Figures 6c and 6e). This response is captured to first order by our dimensionless parameter σ^* , which can be rearranged to show that $\sigma^* \sim L_b / L_{auto}$ (Equation 14). Thereby, σ^* describes whether the backwater-scaled delta will retreat basinward ($L_{auto} < L_b$) or prograde seaward ($L_{auto} > L_b$) before experiencing autoretreat.

Previous work has identified that deltas respond to sea-level rise through the process of autoretreat, wherein the shoreline eventually retreats landward regardless of rise rate. In our simulations, we find that many avulsions occur before there are significant signs of autoretreat (Figures 6a, 6c and 6e) and that avulsion frequency depends on rise rate (σ^*) to first order (Figure 5a). Nevertheless, our results can shed light upon changes to avulsion frequency over autoretreat timescales, because different σ^* runs are analogous to different segments of the autoretreat trajectory (Muto & Steel, 2002) (Figure 13). Over timescales of $T_{auto} \gg T_c$, a delta subject to constant sea-level rise will experience autoretreat because the foreset will grow too large to sustain with the sediment supply (Muto et al., 2007). Our results suggest that the onset of autoretreat will be associated with more frequent avulsions at an upstream-migrating node (Figure 13). So long as there is sufficient sediment to prograde the active lobe, the delta will continue to build back-stepping lobes and avulse during shoreline transgression—a response that is not captured in 1-D models of autoretreat (Tomer et al., 2011; Wu et al., 2020). The ever-lengthening

with previous work (Chadwick et al., 2019; Moodie et al., 2019; Ratliff et al., 2021). Because avulsions in the backwater zone are unlikely to occur with large H^* , avulsions occur in the trunk channel where aggradation is approximately uniform and driven by long-term progradation (Figure 12c).

5. Discussion

5.1. Comparison to Previous Work on Avulsion Response to Climate Change

Our results support the idea that the avulsion node on backwater-influenced deltas should translate downstream with shoreline progradation (Ganti et al., 2014) and also upstream with shoreline transgression (Figures 6a, 6c and 6e). We observe a slight decrease in avulsion length with increasing rise rate (Figure 5b), which is less pronounced than shown in Chatanantavet et al. (2012) because their model did not incorporate multiple lobes and avulsion cycles that cause autogenic variability. In cases with delta progradation, avulsion-node migration occurs intermittently (Figures 6b and 6d), taking place when the river is forced to aggrade a thicker lobe to achieve adequate superelevation (Figure 4d). This finding is consistent with historical observations of the Yellow River delta, where the avulsion location has intermittently migrated downstream with shoreline progradation over the past century (Ganti et al., 2014). Upstream migration of the backwater zone and avulsion node during sea-level rise has been observed in recent models (Moran et al., 2017; Wu et al., 2020). However, these models only considered the special case where the backwater zone originates from sea-level rise under constant discharge, which is not applicable to most lowland deltas (Chadwick et al., 2019). Our results demonstrate the avulsion node migrates upstream in the more general case, where backwater zones originate from natural variability in river discharge (Chatanantavet et al., 2012; Lamb et al., 2012). Importantly, our findings also challenge the common assumption that avulsion nodes remain geographically fixed during sea-level rise (Jerolmack, 2009; Kim et al., 2006; Paola et al., 2011). Delta size in our model does not adjust to the autostratigraphic length-scale L_{auto} , as Equation 2 suggests. Instead,

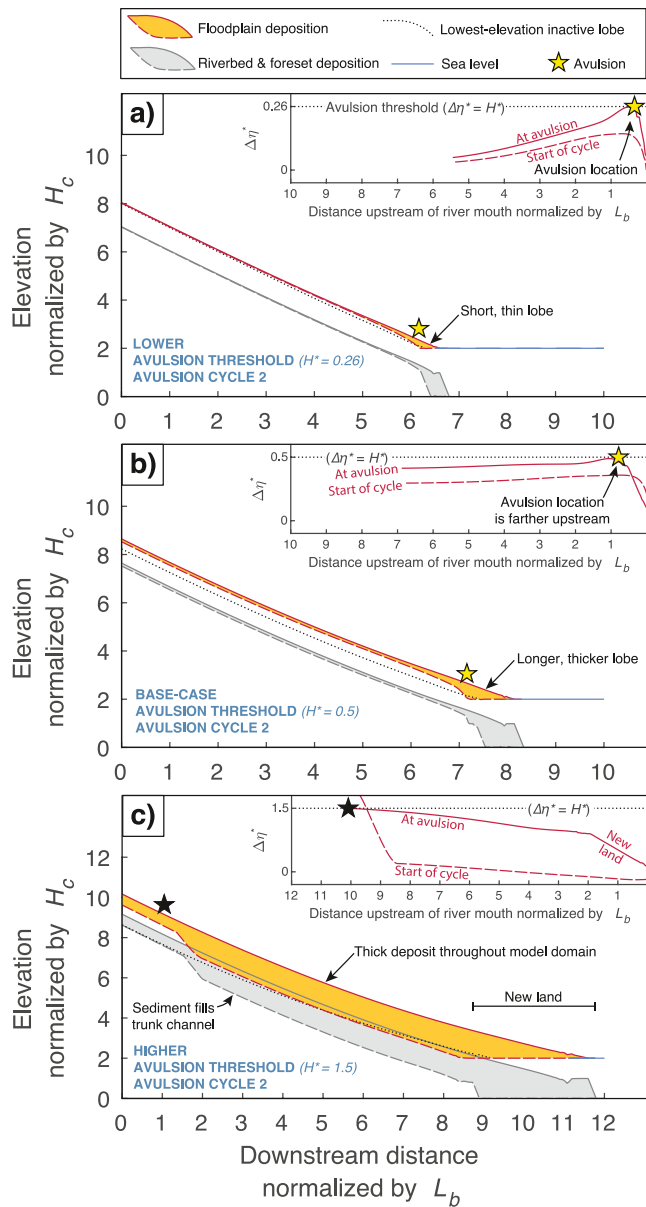


Figure 12. Examples of avulsion cycles under flood regimes with (a) low avulsion threshold $H^* = 0.26$, (b) intermediate avulsion threshold $H^* = 0.5$, and (c) high avulsion threshold $H^* = 1.5$. Shaded regions show deposition on the riverbed and foreset (gray) and on the floodplain (orange) over one avulsion cycle. Floodplain profiles of the active lobe (red lines, shown for the start and end of the avulsion cycle) and the lowest inactive lobe (black dotted line) are used to calculate super-elevation (see inset). Stars show avulsion location, and are color-coded yellow for trunk-bypass avulsion cycles and black for avulsions that occurred in the trunk channel.

be rare when floods are small but occur frequently (i.e., low CV and high F_{bf}), because lobes are larger and aggrade more slowly. Avulsion frequency may be less sensitive to flood regimes with large and frequent floods (i.e., high CV and high F_{bf}), because although aggradation rates are slower, this effect is compensated by the smaller size of lobes.

foreset necessitates that the active lobe will eventually drown, at which point avulsions will cease to occur and the system will experience non-deltaic transgression (Tomer et al., 2011). We expect deltas with different initial basin depths and river lengths to feature altered autoretreat trajectories (Muto & Steel, 2002) and avulsion frequencies (Chadwick et al., 2020), but that large-scale response will remain consistent across deltas.

Our results show that increases in sediment supply can trigger avulsions upstream of the backwater zone. This finding is supported by field observations on the Tacuari megafan (Makaske et al., 2012) and in New Zealand (Korup, 2004), where pulses in sediment supply were linked to inland avulsions. Our results also provide a potential explanation for avulsions deposits far upstream of the Mississippi delta dating to the middle Holocene (Chamberlain et al., 2018; Saucier, 1994). As continental ice sheets melted, increased sediment supply to the Mississippi could have caused avulsions in the trunk channel, in a manner similar to our model results when $\delta Q_s > 0.1$ (Figures 8c–8f). Increased sediment supply also causes more frequent avulsions in our model (Figure 7b), consistent with field observations on the Rhine-Meuse delta (Stouthamer & Berendsen, 2001) and flume experiments (Ashworth et al., 2004; Bryant et al., 1995). We reason that $\delta Q_s > 0.1$ is likely not a universal threshold for all deltas, because the evolution of the depositional wave should depend on grain size, Shields number, and Froude number which vary from river to river. Furthermore, the shift to upstream avulsions should also depend on the trunk channel length downstream of the sediment input, which affects the transit time for the wave to propagate to the backwater zone. We expect that, after the wave disperses and the river reaches a new equilibrium slope, avulsions should again resume in the backwater zone, as we observe in $\delta Q_s < 0.1$ runs (Figures 8a and 8b). However, we do not observe a return to equilibrium conditions for cases with $\delta Q_s > 0.1$ over the nine avulsion cycles considered, in part because avulsions in the trunk channel interrupt downstream slope adjustment by distributing sediment laterally among lobes (Figures 8c and 8e).

We identify two effects of flood regime on avulsion frequency. First, increased flood frequency F_{bf} causes less frequent avulsions (Figure 10d) by promoting scour in the backwater zone and lowering long-term aggradation rates (Figure 11). Second, reduced avulsion threshold, H^* , reduces the size of lobes, allowing for more frequent avulsions (Figures 10h and 12). Field data suggest H^* is lower for deltas with higher stage-height variability CV (Ganti et al., 2014). Thus, while we do not find a direct effect from CV on avulsion frequency (Figure 10b), our results suggest that increased CV can indirectly enhance avulsion frequency by reducing H^* . Our model runs isolate the effect of F_{bf} , H^* , and CV , but in nature these flood parameters may co-vary with climate. We reason that avulsions occur most frequently when floods are large but infrequent (i.e., high CV and low F_{bf}), because this allows for rapid aggradation of relatively small delta lobes. Conversely, avulsions should

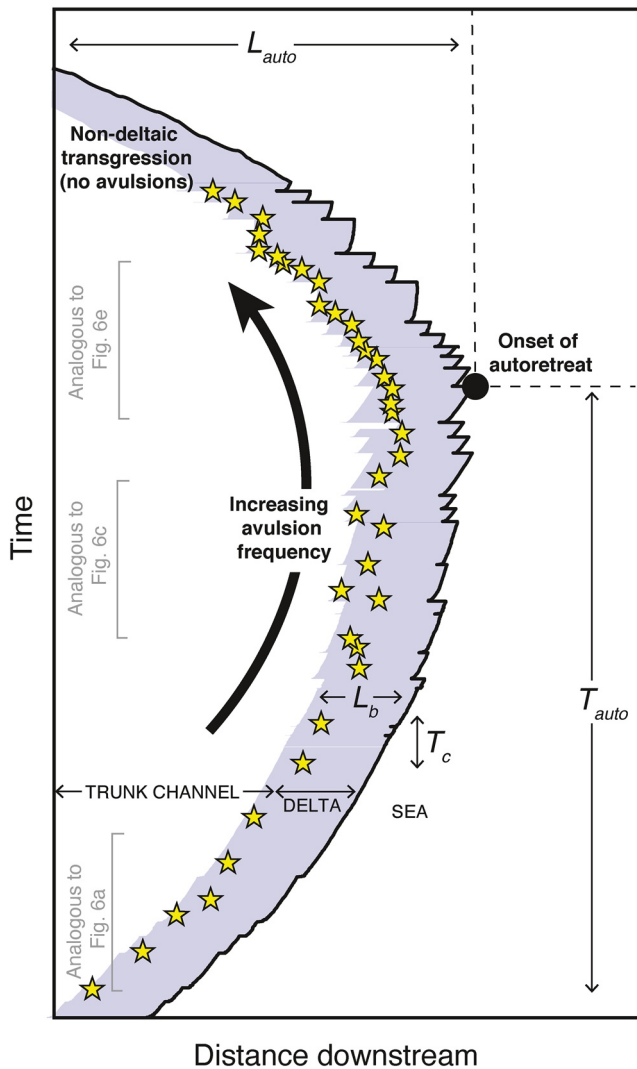


Figure 13. Hypothetical result for avulsions over an autoretreat trajectory, through analogy with Figure 6. Black line is the shoreline of the active lobe, stars are avulsions, and blue shaded area indicates the backwater zone. Avulsions occur within the backwater zone of length L_b over timescales of T_c . The autostratigraphic length-scale L_{auto} and timescale T_{auto} estimate where and when autoretreat begins. During autoretreat, avulsions are expected to grow more frequent and shift landward.

5.2. Implications for Avulsions During Glacial-Interglacial Cycles

Our results provide new insight for how avulsion patterns change over glacial-interglacial cycles (Figures 14a and 14b). Continental glaciation is associated with global sea-level fall, reduced runoff, and potentially reduced sediment supply (Blum & Törnqvist, 2000; Hovius, 1998). According to our model, these conditions facilitate persistent backwater-scaled avulsions (Figure 14a), granted that the backwater zone remains aggradational (Figure 5) (Chadwick et al., 2020; T. I. Lane et al., 2017; Nijhuis et al., 2015). Sea-level fall is often thought to cause river incision, forming incised valleys (Posamentier et al., 1992; Van Wagoner et al., 1988; Zaitlin et al., 1994). However, even within an incised valley, the delta foreset can continue to prograde. Progradation rates increase as the offshore basin shallows (Bijkerk et al., 2016; Chadwick et al., 2020), which may counteract incision and allow backwater-scaled aggradation and avulsion to occur.

As glaciers melt and global sea level rises, delta response depends on the rise rate relative to the aggradation rate (σ^*). For rise rates typical of the most recent interglacial period ($0.1 \lesssim \sigma^* \lesssim 2.5$; Table 1), deltas are expected to shift inland while maintaining a backwater-scaled avulsion node that experiences more frequent avulsions (Figures 5 and 14b). Delta size is not predicted to shrink, as suggested by earlier models (Jerolmack, 2009; Paola et al., 2011), but instead remain relatively constant because the avulsion node moves with the shoreline (Figure 6). Our results also indicate that rapid rise may suppress avulsions if aggradation is insufficient to keep pace with sea-level rise ($\sigma^* \gtrsim 2.5$). Such conditions may have been met during the glacial-interglacial transition ($\sim 20 - 7$ ka), as rise rates were roughly tenfold the interglacial rate (Bintanja et al., 2005; Fleming et al., 1998) and delta-lobe deposits dating to this period are relatively rare (Coleman et al., 1998; Giosan et al., 2006; Nijhuis et al., 2015). Interglacial periods are also potentially associated with increased sediment yield (Blum & Törnqvist, 2000; Hovius, 1998). If the sediment yield increased enough for trunk channel aggradation to outpace backwater zone aggradation ($\delta Q_c > 0.1$ in our model), we expect climate change could trigger avulsions far upstream in the trunk channel (Figures 7a and 14b). Furthermore, increased overbank flood frequency (Knox, 2000; Munoz et al., 2018) could cause less frequent avulsions (Figure 10d). Thus, avulsions upstream of the backwater zone should be more common during interglacial periods, and the drowned continental shelf could contain deposits and erosional surfaces (Ganti et al., 2019; Trower et al., 2018) that reflect relict backwater-scaled avulsion nodes formed during the last glacial period (Figures 14a and 14b).

5.3. Implications for Avulsions During Anthropogenic Climate Change

Global sea level is rising at an accelerating pace and, combined with coastal subsidence, is expected to induce landward retreat of the shoreline on many deltas over the next century (Figures 14c and 14d) (Chadwick et al., 2020; Ericson et al., 2006; Pachauri et al., 2014; Syvitski et al., 2009). Our simulations predict shoreline retreat will be associated with upstream migration of avulsion locations (Figure 6e), with potentially disastrous consequences. For example, the Old River Control Structure, a billion-dollar project that prevented avulsion of the Mississippi River (Kenney et al., 2013), may be rendered obsolete if the avulsion node migrates upstream of the structure. In such a scenario, avulsion-mitigation efforts will need to be implemented upstream in order to protect inland communities from new avulsion hazards. Our results

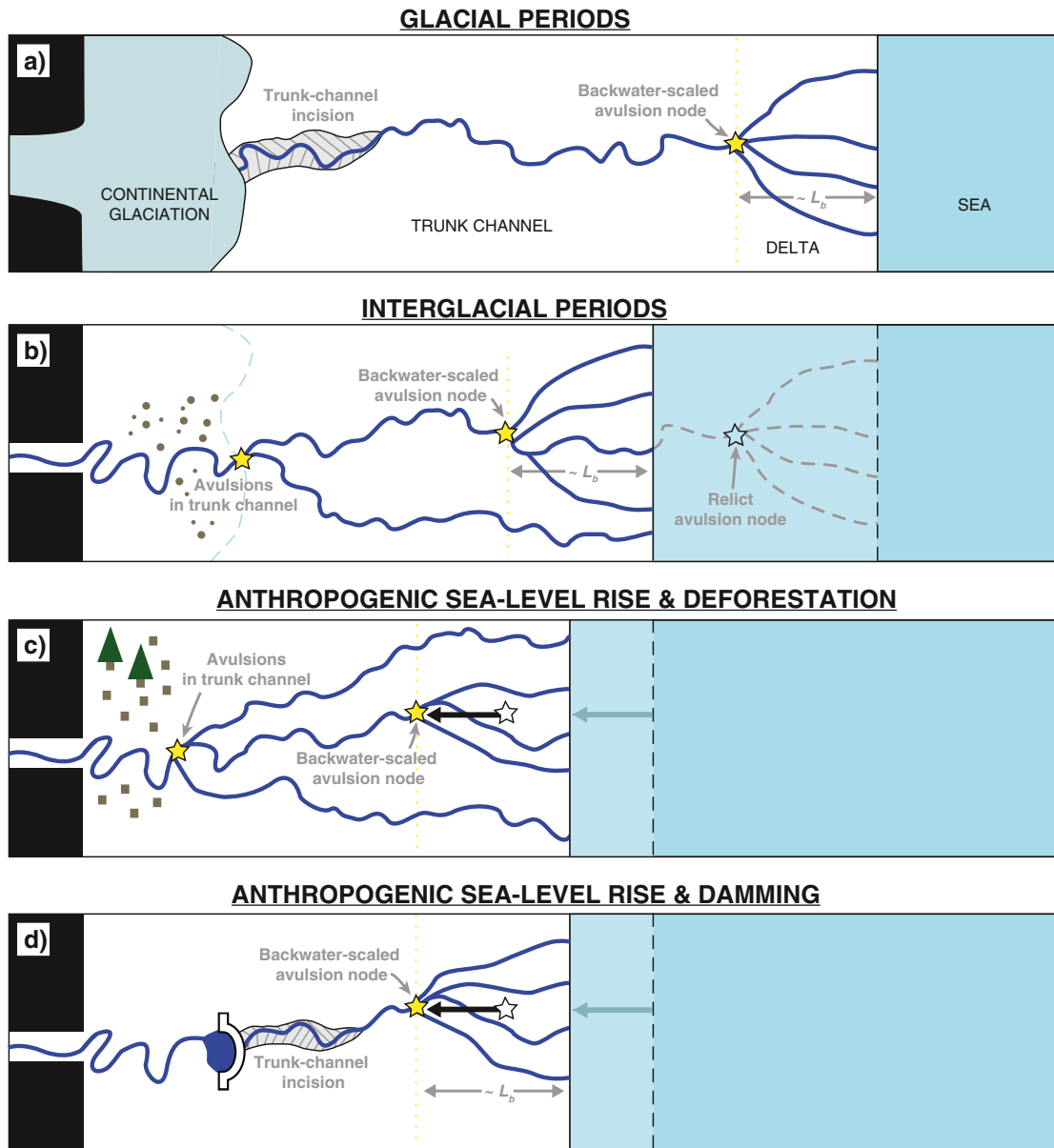


Figure 14. Schematics of delta response to climate change during (a) glacial periods, (b) interglacial periods, and (c–d) anthropogenic climate change. (c) Expected response for deltas where sediment supply increases due to deforestation. (d) Expected response for deltas where sediment supply decreases due to damming.

also support existing models that avulsions will occur more frequently due to accelerated relative sea-level rise (Figure 5a) (Chadwick et al., 2020; Chatanantavet et al., 2012; Jerolmack, 2009). Modern estimates of σ^* indicate that most deltas remain in the regime where the active lobe continues to aggrade and avulse ($\sigma^* < 2.5$) (Chadwick et al., 2020).

On some deltas, relative sea-level rise is occurring in concert with increases to riverine sediment supply, primarily due to deforestation and agricultural land use (Giosan et al., 2012; Jenny et al., 2019; Nienhuis et al., 2020). Our model predicts rivers may respond to enhanced sediment supply by avulsing far upstream of the pre-existing avulsion node, in the trunk channel (Figure 14c). Other deltas are experiencing reduced sediment supply due to dams (Giosan et al., 2011; Syvitski & Saito, 2007; Zhou et al., 2015). Our results suggest that avulsion location and frequency should be insensitive to these effects—at least for dams situated in

the trunk channel. While the trunk channel may incise immediately downstream of the dam, the delta can still build seaward and aggrade (Figure 9d) such that avulsions are relatively unaffected (Figure 7).

Dams also affect flood frequency and magnitude (Leopold & Maddock, 1954). While dams are typically designed to restrict the occurrence of overbank floods (F_{bf}) in order to mitigate flood risks, our results indicate an unintended consequence that avulsions will occur more frequently (Figure 10d); without periodic scour caused by floods, channels will aggrade more rapidly in the backwater zone. Therefore, frequent, controlled floods can be an effective management strategy to mitigate avulsion risks on deltas, as has been demonstrated on the Yellow River delta, China (Wang et al., 2017). Regardless of dam management, anthropogenic climate change is causing more frequent and more extreme storm events (Estrada et al., 2015; Lin et al., 2012; Munoz et al., 2018). Our model results indicate that increased flood frequency (F_{bf}) can cause less frequent avulsions (Figure 10d), but that increased flood magnitude (CV) can potentially offset this effect by reducing H^* thereby causing more frequent avulsions (Figure 10h). We reason that avulsions could become more or less frequent depending on the specific flood regime (Blum & Törnqvist, 2000; Knox & Wright, 1983; Langbein & Schumm, 1958). Even deltas with reduced avulsion frequency will face new avulsion hazards: as avulsions become less frequent, avulsion length is also expected to increase (Figures 10c and 10g), which would introduce new avulsion hazards upstream.

Our results show that most avulsions occur within the backwater zone (trunk-bypass avulsions), and that these avulsions have a statistically characteristic frequency and location. The model also shows the possibility for rare avulsions in the trunk channel that could be unexpected and devastating (Figure 4). Hiatuses in deltaic avulsions due to trunk-channel aggradation are not uncommon in our simulations (33% of all avulsions) and may be particularly important to identify: they are capable of temporarily reducing both avulsion hazards and land-building potential for 10–1,000 yr, until the trunk channel has adjusted. Deltas undergoing trunk-filling avulsion cycles should exhibit comparable aggradation rates between the trunk channel and deltaic channels. In contrast, during trunk-bypass avulsion cycles, aggradation rates are much lower in the trunk channel compared to the delta (Figures 4c and 4d).

6. Conclusions

We use a morphodynamic model for repeated delta-lobe construction and avulsion to explore how climate change affects avulsion frequency and location considering both upstream and downstream controls. At the downstream end, sea-level rise causes more frequent avulsions at a distance from the shoreline set by the backwater length-scale (Figure 5). Because avulsion length remains relatively constant, the avulsion node migrates seaward during shoreline progradation, and migrates landward during shoreline retreat (Figure 6). At the upstream end, significant increases to sediment supply are capable of causing avulsions in the trunk channel, upstream of the backwater zone (Figures 7a and 8). Reduced sediment supply has comparatively little impact on deltaic avulsions (Figure 7), because despite trunk-channel incision the delta adjusts its transport slope via progradation and aggradation (Figures 9c and 9d). With regards to flood regime, avulsion frequency is inversely correlated with overbank flood frequency (Figure 10d), but positively correlated with stage-height variability via reduction of H^* (Figure 10h), due to competing effects on aggradation rate and lobe thickness.

Overall, our findings demonstrate that deltaic avulsions are sensitive to both upstream and downstream controls associated with climate change. Results suggest that deltas shift landward and seaward over glacio-eustatic sea-level cycles, leaving behind relict backwater-scaled avulsion nodes on drowned continental shelves (Figures 14a and 14b). Interglacial periods should be marked by more frequent avulsions due to sea-level rise, and also upstream avulsions in the trunk channel during pulses in sediment supply. Finally, our results warn of the impact of anthropogenic climate change and land use on avulsion hazards. Accelerated relative sea-level rise threatens to drown coastal wetlands, pushing the avulsion node upstream and causing more frequent avulsions (Figures 14c and 14d). Deforestation and agricultural practices can increase sediment supply, promoting trunk channel avulsions near the sediment source. Avulsions are also sensitive to modern changes in flood regime which, due to trade-offs between aggradation rate and lobe

size, could induce either more frequent avulsions closer to the shore, or less frequent avulsions farther inland, depending on the delta in question (Figure 10).

Notation

B	Flow width [L]
B_c	Channel width [L]
B_f	Floodplain/lobe width [L]
C_f	Friction factor [-]
CV	Coefficient of variation of stage height [-]
D	Median grain size of bed material [L]
f_A	Avulsion frequency [1/T]
f_A^*	Normalized avulsion frequency [-]
F_{bf}	Bankfull exceedance probability [-]
Fr	Froude number [-]
$Fr_{n,bf}$	Bankfull Froude number in the normal-flow reach [-]
g	Acceleration due to gravity [L/T ²]
H	Flow depth [L]
H^*	Avulsion threshold [-]
H_b	Offshore basin depth [L]
H_c	Channel depth [L]
L_A	Avulsion length (also known as delta size) [L]
L_A^*	Normalized avulsion length [-]
L_{auto}	Autostratigraphic length-scale [L]
L_b	Backwater length-scale [L]
n	Average number of avulsions before lobe reoccupation [-]
N	Number of delta lobes [-]
P	Probability distribution of flow regime [-]
q_s	Width-averaged sediment supply [L ² /T]
\bar{Q}_s	Sediment supply [L ³ /T]
\bar{Q}_s	Time-averaged sediment supply [L ³ /T]
\bar{Q}_t	Sediment transport capacity of total bed-material load [L ³ /T]
\bar{Q}_{t0}	Time-averaged initial sediment transport capacity [L ³ /T]
Q_w	Water discharge [L ³ /T]
R	Submerged specific gravity of sediment [-]
S	Riverbed slope [-]
S_a	Foreset avalanche slope [-]
S_0	Transport slope at the ghost node [-]
t	Time [T]
T_A	Time between avulsions [T]
T_{auto}	Autostratigraphic time-scale [T]
T_c	Channel-filling time-scale [T]
T_e	Flood event duration [T]
v_a	Aggradation rate [L/T]
x	Downstream distance [L]
x_A	Downstream distance of avulsion site [L]
x_m	Downstream distance of river mouth [L]
x_{tf}	Downstream distance of topset-foreset break [L]
α	Coefficient in Equation 6 [-]
β	Exponent in Equation 6 [-]
$\Delta\eta$	Superelevation [L]
η	Riverbed elevation [L]
η_0	Initial riverbed elevation [L]
$\eta_{abandoned}$	Riverbed elevation on abandoned lobe [L]

η_f	Floodplain elevation [L]
$\eta_{f,abandoned}$	Floodplain elevation on abandoned lobe [L]
η_{new}	New riverbed elevation after avulsion [L]
λ_p	Sediment porosity in lobe deposit [-]
Λ	Ratio of wash load to bed-material load in lobe deposit [-]
Ω	Channel sinuosity [-]
σ	Sea-level rise rate [L/T]
τ^*	Shields number [-]
$\tau_{n,bf}^*$	Bankfull Shields number in the normal-flow reach [-]
ζ_{sea}	Sea level [L]

Conflict of Interest

The authors declare no conflict of interest.

Data Availability Statement

The data and model code underlying this study are publicly available in the SEAD repository (<http://doi.org/10.26009/s0VZMEPD>) and Zenodo (<https://doi.org/10.5281/zenodo.4265479>) respectively.

Acknowledgments

The authors thank Vamsi Ganti, Andrew Moodie, Gary Parker, and Brad Murray for useful discussions. The authors acknowledge NSF Grant EAR 1427262 and the Resnick Sustainability Institute at the California Institute of Technology for support.

References

- Arkesteijn, L., Blom, A., Czapiga, M. J., Chavarrias, V., & Labeur, R. J. (2019). The quasi-equilibrium longitudinal profile in backwater reaches of the engineered Alluvial river: A space-marching method. *Journal of Geophysical Research: Earth Surface*, *124*(11), 2542–2560. <https://doi.org/10.1029/2019JF005195>
- Ashworth, P. J., Best, J. L., & Jones, M. (2004). Relationship between sediment supply and avulsion frequency in braided rivers. *Geology*, *32*(1), 21–24. <https://doi.org/10.1130/g19919.1>
- Bianchi, T. S., & Allison, M. A. (2009). Large-river delta-front estuaries as natural “recorders” of global environmental change. *Proceedings of the National Academy of Sciences*, *106*(20), 8085–8092. <https://doi.org/10.1073/pnas.0812878106>
- Bijkerk, J. F., Eggenhuisen, J. T., Kane, I. A., Meijer, N., Waters, C. N., Wignall, P. B., & McCaffrey, W. D. (2016). Fluvio-marine sediment partitioning as a function of basin water depth. *Journal of Sedimentary Research*, *86*(3), 217–235. <https://doi.org/10.2110/jsr.2016.9>
- Bintanja, R., van de Wal, R. S. W., & Oerlemans, J. (2005). Modeled atmospheric temperatures and global sea levels over the past million years. *Nature*, *437*(7055), 125–128. <https://doi.org/10.1038/nature03975>
- Blum, M. D., & Törnqvist, T. E. (2000). Fluvial responses to climate and sea-level change: A review and look forward. *Sedimentology*, *47*, 2–48. <https://doi.org/10.1046/j.1365-3091.2000.00008.x>
- Brizga, S. O., & Finlayson, B. L. (1990). Channel avulsion and river metamorphosis: The case of the Thomson river, Victoria, Australia. *Earth Surface Processes and Landforms*, *15*(5), 391–404. <https://doi.org/10.1002/esp.3290150503>
- Brooke, S. A. S., Ganti, V., Chadwick, A. J., & Lamb, M. P. (2020). Flood variability determines the location of lobe-scale Avulsions on Deltas: Madagascar. *Geophysical Research Letters*, *47*(20), e2020GL088797. <https://doi.org/10.1029/2020gl088797>
- Bryant, M., Falk, P., & Paola, C. (1995). Experimental study of avulsion frequency and rate of deposition. *Geology*, *23*(4), 365–368. [https://doi.org/10.1130/0091-7613\(1995\)023<0365:esoafa>2.3.co;2](https://doi.org/10.1130/0091-7613(1995)023<0365:esoafa>2.3.co;2)
- Carlson, B., Piliouras, A., Muto, T., & Kim, W. (2018). Control of basin water depth on channel morphology and autogenic timescales in deltaic systems. *Journal of Sedimentary Research*, *88*(9), 1026–1039. <https://doi.org/10.2110/jsr.2018.52>
- Chadwick, A. J., Lamb, M. P., & Ganti, V. (2020). Accelerated river avulsion frequency on lowland deltas due to sea-level rise. *Proceedings of the National Academy of Sciences*, *117*, 17584–17590. <https://doi.org/10.1073/pnas.1912351117>
- Chadwick, A. J., Lamb, M. P., Moodie, A. J., Parker, G., & Nittrouer, J. A. (2019). Origin of a preferential avulsion node on lowland river deltas. *Geophysical Research Letters*, *46*(8), 4267–4277. <https://doi.org/10.1029/2019gl082491>
- Chamberlain, E. L., Törnqvist, T. E., Shen, Z., Mauz, B., & Wallinga, J. (2018). Anatomy of Mississippi Delta growth and its implications for coastal restoration. *Science Advances*, *4*(4), eaar4740. <https://doi.org/10.1126/sciadv.aar4740>
- Chatanantavet, P., & Lamb, M. P. (2014). Sediment transport and topographic evolution of a coupled river and river plume system: An experimental and numerical study. *Journal of Geophysical Research: Earth Surface*, (Figure 1), *119*(6), 1263–1282. <https://doi.org/10.1002/2013JF002810>
- Chatanantavet, P., Lamb, M. P., & Nittrouer, J. A. (2012). Backwater controls of avulsion location on deltas. *Geophysical Research Letters*, *39*(1). <https://doi.org/10.1029/2011GL050197>
- Chow, V. T. (1959). Gradually Varied Flow: Theory and Analysis. In *Open-channel hydraulics*, McGraw-Hill.
- Coleman, J. M., Roberts, H. H., & Stone, G. W. (1998). Mississippi River delta: An overview. *Journal of Coastal Research*, *14*(3).
- Engelund, F., & Hansen, E. (1967). A Monograph on Sediment Transport in Alluvial Streams (Vol. 10). Copenhagen K: Technical University of Denmark Østervoldgade.
- Ericson, J., Vörösmarty, C., Dingman, S., Ward, L., & Meybeck, M. (2006). Effective sea-level rise and deltas: Causes of change and human dimension implications. *Global and Planetary Change*, *50*(1–2), 63–82. <https://doi.org/10.1016/j.gloplacha.2005.07.004>
- Estrada, F., Botzen, W. J. W., & Tol, R. S. J. (2015). Economic losses from US hurricanes consistent with an influence from climate change. *Nature Geoscience*, *8*(11), 880–884. <https://doi.org/10.1038/ngeo2560>
- Fisk, H. N. (1945). *Geological investigation of the alluvial valley of the Lower Mississippi River*. Vicksburg, MS: Army Corp of Engineers.

- Fleming, K., Johnston, P., Zwartz, D., Yokoyama, Y., Lambeck, K., & Chappell, J. (1998). Refining the eustatic sea-level curve since the Last Glacial Maximum using far- and intermediate-field sites. *Earth and Planetary Science Letters*, 163(1–4), 327–342. [https://doi.org/10.1016/S0012-821X\(98\)00198-8](https://doi.org/10.1016/S0012-821X(98)00198-8)
- Galloway, W. E. (1975). Process framework for describing the morphologic and stratigraphic evolution of deltaic depositional systems. In M. L. Broussard (Ed.), *Deltas: Models for Exploration* (pp. 87–98). Houston Geological Society.
- Ganti, V., Chadwick, A. J., Hassenruck-Gudipati, H. J., Fuller, B. M., & Lamb, M. P. (2016). Experimental river delta size set by multiple floods and backwater hydrodynamics. *Science Advances*, 2(5), e1501768. <https://doi.org/10.1126/sciadv.1501768>
- Ganti, V., Chadwick, A. J., Hassenruck-Gudipati, H. J., & Lamb, M. P. (2016). Avulsion cycles and their stratigraphic signature on an experimental backwater-controlled delta. *Journal of Geophysical Research: Earth Surface*, 121(9), 1651–1675. <https://doi.org/10.1002/2016JF003915>
- Ganti, V., Chu, Z., Lamb, M. P., Nittrouer, J. A., & Parker, G. (2014). Testing morphodynamic controls on the location and frequency of river avulsions on fans versus deltas: Huanghe (Yellow River), China. *Geophysical Research Letters*, 41, 7882–7890. <https://doi.org/10.1002/2014GL061918>
- Ganti, V., Lamb, M. P., & Chadwick, A. J. (2019). Autogenic erosional surfaces in fluvio-deltaic stratigraphy from floods, avulsions, and backwater hydrodynamics. *Journal of Sedimentary Research*, 89(8), 815–832. <https://doi.org/10.2110/jsr.2019.40>
- Giosan, L., Coolen, M. J. L., Kaplan, J. O., Constantinescu, S., Filip, F., Filipova-Marinova, M., et al. (2012). Early anthropogenic transformation of the Danube-Black Sea system. *Scientific Reports*, 2, 582. <https://doi.org/10.1038/srep00582>
- Giosan, L., Donnelly, J. P., Constantinescu, S., Filip, F., Ovejanu, I., Vespremeanu-Stroe, A., et al. (2006). Young Danube delta documents stable Black Sea level since the middle Holocene: Morphodynamic, paleogeographic, and archeological implications. *Geology*, 34(9), 757–760. <https://doi.org/10.1130/G22587.1>
- Giosan, L., Donnelly, J. P., Vespremeanu, E., Bhattacharya, J. P., Olariu, C., & Buonaiuto, F. S. (2011). River delta morphodynamics: Examples from the Danube delta. *River Deltas—Concepts, Models, and Examples*, Special Publications of SEPM (Vol. 83, pp. 393–411). Tulsa, OK: SEPM Society for Sedimentary Geology. <https://doi.org/10.2110/pec.05.83.0393>
- Giosan, L., Syvitski, J., Constantinescu, S., & Day, J. (2014). Protect the world's deltas. *Nature News*, 516(7529), 31–33. <https://doi.org/10.1038/516031a>
- Gleick, P. H. (2003). Global freshwater resources: Soft-path solutions for the 21st century. *Science*, 302(2003), 1524–1528. <https://doi.org/10.1126/science.1089967>
- Hajek, E. A., & Edmonds, D. A. (2014). Is river avulsion style controlled by floodplain morphodynamics? *Geology*, 42(3), 199–202. <https://doi.org/10.1130/G35045.1>
- Hallet, B., Hunter, L., & Bogen, J. (1996). Rates of erosion and sediment evacuation by glaciers: A review of field data and their implications. *Global and Planetary Change*, 12(1–4), 213–235. [https://doi.org/10.1016/0921-8181\(95\)00021-6](https://doi.org/10.1016/0921-8181(95)00021-6)
- Hayden, A. T., Lamb, M. P., Fischer, W. W., Ewing, R. C., McElroy, B. J., & Williams, R. M. E. (2019). Formation of sinuous ridges by inversion of river-channel belts in Utah, USA, with implications for Mars. *Icarus*, 332, 92–110. <https://doi.org/10.1016/j.icarus.2019.04.019>
- Hotchkiss, R. H., & Parker, G. (1991). Shock fitting of aggradational profiles due to backwater. *Journal of Hydraulic Engineering*, 117(9), 1129–1144. [https://doi.org/10.1061/\(asce\)0733-9429\(1991\)117:9\(1129\)](https://doi.org/10.1061/(asce)0733-9429(1991)117:9(1129))
- Hovius, N. (1998). Controls on sediment supply by large rivers. *Relative Role of Eustasy, Climate, and Tectonism in Continental Rocks*. Special Publications of SEPM, (Vol. 59). Tulsa, OK: SEPM Society for Sedimentary Geology. <https://doi.org/10.2110/pec.98.59.0002>
- Howard, A. D. (1982). Equilibrium and time scales in geomorphology: Application to sand-bed alluvial streams. *Earth Surface Processes and Landforms*, 7(4), 303–325. <https://doi.org/10.1002/esp.3290070403>
- Jelgersma, S. (1996). Land subsidence in coastal lowlands. In sea-level rise and coastal subsidence (pp. 47–62). Springer. https://doi.org/10.1007/978-94-015-8719-8_3
- Jenny, J.-P., Koirala, S., Gregory-Eaves, I., Francus, P., Niemann, C., Ahrens, B., et al. (2019). Human and climate global-scale imprint on sediment transfer during the Holocene. *Proceedings of the National Academy of Sciences of the United States of America*, 116(46), 22972–22976. <https://doi.org/10.1073/pnas.1908179116>
- Jerolmack, D. J. (2009). Conceptual framework for assessing the response of delta channel networks to Holocene sea level rise. *Quaternary Science Reviews*, 28(17–18), 1786–1800. <https://doi.org/10.1016/j.quascirev.2009.02.015>
- Jerolmack, D. J., & Mohrig, D. (2007). Conditions for branching in depositional rivers. *Geology*, 35(5), 463. <https://doi.org/10.1130/G23308A.1>
- Jerolmack, D. J., & Swenson, J. B. (2007). Scaling relationships and evolution of distributary networks on wave-influenced deltas. *Geophysical Research Letters*, 34(23). <https://doi.org/10.1029/2007GL031823>
- Kenney, M. A., Hobbs, B. F., Mohrig, D., Huang, H., Nittrouer, J. A., Kim, W., & Parker, G. (2013). Cost analysis of water and sediment diversions to optimize land building in the Mississippi River delta. *Water Resources Research*, 49(6), 3388–3405. <https://doi.org/10.1002/wrcr.20139>
- Kim, W., Paola, C., Voller, V. R., & Swenson, J. B. (2006). Experimental measurement of the relative importance of controls on shoreline migration. *Journal of Sedimentary Research*, 76(2), 270–283. <https://doi.org/10.2110/jsr.2006.019>
- Knox, J. C. (2000). Sensitivity of modern and Holocene floods to climate change. *Quaternary Science Reviews*, 19(1–5), 439–457. [https://doi.org/10.1016/S0277-3791\(99\)00074-8](https://doi.org/10.1016/S0277-3791(99)00074-8)
- Knox, J. C., & Wright, H. E. (1983). Responses of river systems to Holocene climates. *Late Quaternary Environments of the United States*, 2, 26–41.
- Korup, O. (2004). Landslide-induced river channel avulsions in mountain catchments of southwest New Zealand. *Geomorphology*, 63(1–2), 57–80. <https://doi.org/10.1016/j.geomorph.2004.03.005>
- Kostic, S., & Parker, G. (2003). Progradational sand-mud deltas in lakes and reservoirs. Part 1. Theory and numerical modeling. *Journal of Hydraulic Research*, 41(2), 127–140. <https://doi.org/10.1080/00221680309499956>
- Lamb, M. P., Nittrouer, J. A., Mohrig, D., & Shaw, J. (2012). Backwater and river plume controls on scour upstream of river mouths: Implications for fluvio-deltaic morphodynamics. *Journal of Geophysical Research*, 117(F1), F01002. <https://doi.org/10.1029/2011JF002079>
- Lane, E. W. (1955). Importance of fluvial morphology in hydraulic engineering. *Proceedings of the American Society of Civil Engineers*, 81(7), 1–17.
- Lane, T. I., Nanson, R. A., Vakarelov, B. K., Ainsworth, R. B., & Dashtgard, S. E. (2017). *Evolution and Architectural Styles of a Forced-Regressive Holocene Delta and Megafan, Mitchell River, Gulf of Carpentaria, Australia*. T. Geological Society, London, Special Publications (Vol. 444). Geological Society of London.
- Langbein, W. B., & Schumm, S. A. (1958). Yield of sediment in relation to mean annual precipitation. *Eos, Transactions American Geophysical Union*, 39(6), 1076–1084. <https://doi.org/10.1029/tr039i006p01076>

- LeBoutillier, D. W., & Waylen, P. R. (1993). A stochastic model of flow duration curves. *Water Resources Research*, *29*(10), 3535–3541. <https://doi.org/10.1029/93wr01409>
- Leopold, L. B., & Maddock, T. (1953). The hydraulic geometry of stream channels and some physiographic implications (Vol. 252). US Government Printing Office.
- Leopold, L. B., & Maddock, T. (1954). *The flood control controversy: Big dams, little dams, and land management*.
- Liang, M., Van Dyk, C., & Passalacqua, P. (2016). Quantifying the patterns and dynamics of river deltas under conditions of steady forcing and relative sea level rise. *Journal of Geophysical Research: Earth Surface*, *121*(2), 465–496. <https://doi.org/10.1002/2015JF003653>
- Lin, N., Emanuel, K., Oppenheimer, M., & Vanmarcke, E. (2012). Physically based assessment of hurricane surge threat under climate change. *Nature Climate Change*, *2*(6), 462–467. <https://doi.org/10.1038/nclimate1389>
- Mackin, J. H. (1948). Concept of the graded river. *Geological Society of America Bulletin*, *59*(5), 463–512.
- Makaske, B., Maathuis, B. H. P., Padovani, C. R., Stolker, C., Mosselman, E., & Jongman, R. H. G. (2012). Upstream and downstream controls of recent avulsions on the Taquari megafan, Pantanal, south-western Brazil. *Earth Surface Processes and Landforms*, *37*(12), 1313–1326. <https://doi.org/10.1002/esp.3278>
- Martin, J., Sheets, B., Paola, C., & Hoyal, D. (2009). Influence of steady base-level rise on channel mobility, shoreline migration, and scaling properties of a cohesive experimental delta. *Journal of Geophysical Research*, *114*(F3), F03017. <https://doi.org/10.1029/2008JF001142>
- Members, C. (1988). Climatic changes of the last 18,000 years: Observations and model simulations. *Science*, 1043–1052.
- Milliman, J. D., Broadus, J. M., & Gable, F. (1989). Environmental and economic implications of rising sea level and subsiding deltas: The Nile and Bengal examples. *Ambio*, 340–345.
- Milliman, J. D., & Syvitski, J. P. M. (1992). Geomorphic/Tectonic control of sediment discharge to the ocean: The importance of small mountainous rivers. *The Journal of Geology*, *100*(5), 525–544. <https://doi.org/10.1086/629606>
- Mohrig, D., Heller, P. L., Paola, C., & Lyons, W. J. (2000). Interpreting avulsion process from ancient alluvial sequences: Guadalope-Matarranya system (northern Spain) and Wasatch Formation (western Colorado). *Geological Society of America Bulletin*, *112*, 1787–1803. [https://doi.org/10.1130/0016-7606\(2000\)112<1787:iapfaa>2.0.co;2](https://doi.org/10.1130/0016-7606(2000)112<1787:iapfaa>2.0.co;2)
- Moodie, A. J., Nittrouer, J. A., Ma, H., Carlson, B. N., Chadwick, A. J., Lamb, M. P., & Parker, G. (2019). Modeling deltaic lobe-building cycles and channel avulsions for the Yellow River Delta, China. *Journal of Geophysical Research: Earth Surface*, *124*, 2438–2462. <https://doi.org/10.1029/2019JF005220>
- Moran, K. E., Nittrouer, J. A., Perillo, M. M., Lorenzo-Trueba, J., & Anderson, J. B. (2017). Morphodynamic modeling of fluvial channel fill and avulsion time scales during early Holocene transgression, as substantiated by the incised valley stratigraphy of the Trinity River, Texas. *Journal of Geophysical Research: Earth Surface*, *122*(1), 215–234. <https://doi.org/10.1002/2015JF003778>
- Munoz, S. E., Giosan, L., Therrell, M. D., Remo, J. W. F., Shen, Z., Sullivan, R. M., et al. (2018). Climatic control of Mississippi River flood hazard amplified by river engineering. *Nature*, *556*(7699), 95–98. <https://doi.org/10.1038/nature26145>
- Muto, T. (2001). Shoreline autoretreat substantiated in flume experiments. *Journal of Sedimentary Research*, *71*(2), 246–254. <https://doi.org/10.1306/091400710246>
- Muto, T., Furubayashi, R., Tomer, A., Sato, T., Kim, W., Naruse, H., & Parker, G. (2016). Planform evolution of deltas with graded alluvial topsets: Insights from three-dimensional tank experiments, geometric considerations and field applications. *Sedimentology*, *63*(7), 2158–2189. <https://doi.org/10.1111/sed.12301>
- Muto, T., & Steel, R. J. (1997). Principles of regression and transgression: The nature of the interplay between accommodation and sediment supply. *Journal of Sedimentary Research*, *67*(6, B), 994–1000. <https://doi.org/10.1306/D42686A8-2B26-11D7-8648000102C1865D>
- Muto, T., & Steel, R. J. (2002). Role of autoretreat and A/S changes in the understanding of deltaic shoreline trajectory: A semi-quantitative approach. *Basin Research*, *14*(3), 303–318. <https://doi.org/10.1046/j.1365-2117.2002.00179.x>
- Muto, T., Steel, R. J., & Swenson, J. B. (2007). Autostratigraphy: A framework norm for genetic stratigraphy. *Journal of Sedimentary Research*, *77*(1–2), 2–12. <https://doi.org/10.2110/jsr.2007.005>
- Naito, K., & Parker, G. (2019). Can Bankfull discharge and Bankfull channel characteristics of an Alluvial Meandering River be Cospecified from a flow duration curve? *Journal of Geophysical Research: Earth Surface*, *124*(10), 2381–2401. <https://doi.org/10.1029/2018jfo04971>
- Nicholas, A. P., Aalto, R. E., Sambrook Smith, G. H., & Schwendel, A. C. (2018). Hydrodynamic controls on alluvial ridge construction and avulsion likelihood in meandering river floodplains. *Geology*, *46*(7), 639–642. <https://doi.org/10.1130/g40104.1>
- Nienhuis, J. H., Ashton, A. D., Edmonds, D. A., Hoitink, A. J. F., Kettner, A. J., Rowland, J. C., & Törnqvist, T. E. (2020). Global-scale human impact on delta morphology has led to net land area gain. *Nature*, *577*(7791), 514–518. <https://doi.org/10.1038/s41586-019-1905-9>
- Nijhuis, A. G., Edmonds, D. A., Caldwell, R. L., Cederberg, J. A., Slingerland, R. L., Best, J. L., et al. (2015). Fluvio-deltaic avulsions during relative sea-level fall. *Geology*, *43*(8), 719–722. <https://doi.org/10.1130/g36788.1>
- Olson, D. M., & Dinerstein, E. (1998). The global 200: A representation approach to conserving the Earth's most biologically valuable ecoregions. *Conservation Biology*, *12*(3), 502–515. <https://doi.org/10.1046/j.1523-1739.1998.012003502.x>
- Pachauri, R. K., IPCC & Core Writing Team. (2014). L. A Meyer (Ed.), *Climate Change 2014: Synthesis report. Contribution of Working Groups I, II, III to the Fifth Assessment Report of the Intergovernmental Panel on Climate Change*. Geneva, Switzerland: IPCC.
- Pang, J., & Si, S. (1979). Evolution of the Yellow River mouth: I. Historical shifts. *Oceanologia Et Limnologia Sinica*, *10*(2), 136–141.
- Paola, C., & Mohrig, D. (1996). Palaeohydraulics revisited: Palaeoslope estimation in coarse-grained braided rivers. *Basin Research*, *8*(3), 243–254. <https://doi.org/10.1046/j.1365-2117.1996.00253.x>
- Paola, C., Twilley, R. R., Edmonds, D. A., Kim, W., Mohrig, D., Parker, G., et al. (2011). Natural Processes in delta restoration: Application to the Mississippi Delta. *Annual Review of Marine Science*, *3*(1), 67–91. <https://doi.org/10.1146/annurev-marine-120709-142856>
- Parker, G. (2004). *1D sediment transport morphodynamics with applications to rivers and turbidity currents*. E-Book Available from http://hydrolab.illinois.edu/people/parkerg/morphodynamics_e-book.htm
- Parker, G., Muto, T., Akamatsu, Y., Dietrich, W. E., & Lauer, J. W. (2008). Unraveling the conundrum of river response to rising sea-level from laboratory to field. Part II. The Fly-Strickland River system, Papua New Guinea. *Sedimentology*, *55*(6), 1657–1686. <https://doi.org/10.1111/j.1365-3091.2008.00962.x>
- Posamentier, H. W., Allen, G. P., James, D. P., & Tesson, M. (1992). Forced regressions in a sequence stratigraphic framework: Concepts, examples, and exploration significance. *AAPG Bulletin*, *76*(11), 1687–1709.
- Powell, J. W. (1875). *Exploration of the Colorado River of the West and its Tributaries*. Washington D.C.: Government Printing Office. <https://doi.org/10.3133/70039238>
- Ratliff, K. M., Hutton, E. H. W., & Murray, A. B. (2018). Exploring wave and sea-level rise effects on delta morphodynamics With a coupled river-ocean model. *Journal of Geophysical Research: Earth Surface*, *123*(11), 2887–2900. <https://doi.org/10.1029/2018JF004757>
- Ratliff, K. M., Hutton, E. W. H., & Murray, A. B. (2021). Modeling long-term delta dynamics reveals persistent geometric river avulsion locations. *Earth and Planetary Science Letters*, *559*, 116786. <https://doi.org/10.1016/j.epsl.2021.116786>

- Reitz, M. D., & Jerolmack, D. J. (2012). Experimental alluvial fan evolution: Channel dynamics, slope controls, and shoreline growth. *Journal of Geophysical Research*, *117*(F2), F02021. <https://doi.org/10.1029/2011JF002261>
- Saucier, R. T. (1994). *Geomorphology and quaternary geologic history of the lower Mississippi Valley*. (Vol. 2, p. 363). Vicksburg: US Army Corps of Engineers.
- Schumm, S. A. (1993). River response to baselevel change: Implications for sequence stratigraphy. *The Journal of Geology*, *101*(2), 279–294. <https://doi.org/10.1086/648221>
- Slingerland, R., & Smith, N. D. (2004). River avulsions and their deposits. *Annual Review of Earth and Planetary Sciences*, *32*(1), 257–285. <https://doi.org/10.1146/annurev.earth.32.101802.120201>
- Stanley, D. J., & Warne, A. G. (1994). Worldwide initiation of Holocene marine deltas by deceleration of sea-level rise. *Science*, *265*(5169), 228–231. <https://doi.org/10.1126/science.265.5169.228>
- Stedinger, J. R., Vogel, R. M., & Foufoula-Georgiou, E. (1993). Frequency analysis of extreme events. In D. R. Maidment (Ed.), *Handbook of hydrology* (18.1–18.66). New York, NY: McGraw-Hill.
- Stouthamer, E., & Berendsen, H. J. A. (2001). Avulsion frequency, avulsion duration, and interavulsion period of Holocene Channel Belts in the Rhine-Meuse Delta, The Netherlands. *Journal of Sedimentary Research*, *71*(4), 589–598. <https://doi.org/10.1306/112100710589>
- Sturm, T. W. (2001). *Open Channel Hydraulics*. New York, NY: McGraw-Hill.
- Swenson, J. B., Paola, C., Pratson, L., Voller, V. R., & Murray, B. A. (2005). Fluvial and marine controls on combined subaerial and subaqueous delta progradation: Morphodynamic modeling of compound-clinof orm development. *Journal of Geophysical Research: Earth Surface*, *110*(F2). <https://doi.org/10.1029/2004jf000265>
- Swenson, J. B., Voller, V. R., Paola, C., Parker, G., & Marr, J. G. (2000). Fluvio-deltaic sedimentation: A generalized Stefan problem. *European Journal of Applied Mathematics*, *11*(5), 433–452. <https://doi.org/10.1017/S0956792500004198>
- Syvitski, J. P. M. (2008). Deltas at risk. *Sustainability Science*, *3*(1), 23–32. <https://doi.org/10.1007/s11625-008-0043-3>
- Syvitski, J. P. M., Kettner, A. J., Overeem, I., Hutton, E. W. H., Hannon, M. T., Brakenridge, G. R., et al. (2009). Sinking deltas due to human activities. *Nature Geoscience*, *2*(10), 681–686. <https://doi.org/10.1038/ngeo629>
- Syvitski, J. P. M., & Saito, Y. (2007). Morphodynamics of deltas under the influence of humans. *Global and Planetary Change*, *57*(3–4), 261–282. <https://doi.org/10.1016/j.gloplacha.2006.12.001>
- Tomer, A., Muto, T., & Kim, W. (2011). Autogenic hiatus in fluviodeltaic successions: Geometrical modeling and physical experiments. *Journal of Sedimentary Research*, *81*(3), 207–217. <https://doi.org/10.2110/jsr.2011.19>
- Törnqvist, T. E. (1994). Middle and late Holocene avulsion history of the River Rhine (Rhine-Meuse delta, Netherlands). *Geology*, *22*(8), 711–714.
- Törnqvist, T. E., Wallace, D. J., Storms, J. E. A., Wallinga, J., Van Dam, R. L., Blaaauw, M., et al. (2008). Mississippi Delta subsidence primarily caused by compaction of Holocene strata. *Nature Geoscience*, *1*(3), 173–176. <https://doi.org/10.1038/ngeo129>
- Trower, E. J., Ganti, V., Fischer, W. W., & Lamb, M. P. (2018). Erosional surfaces in the upper Cretaceous Castlegate Sandstone (Utah, USA): Sequence boundaries or autogenic scour from backwater hydrodynamics? *Geology*, *46*(8), 707–710. <https://doi.org/10.1130/g40273.1>
- Van Wagoner, J. C., Posamentier, H. W., Mitchum, R. M. J., Vail, P. R., Sarg, J. F., Loutit, T. S., & Hardenbol, J. (1988). An overview of the fundamentals of sequence stratigraphy and key definitions. *Sea-Level Changes: An Integrated Approach*, Special Publications of SEPM, (Vol. 42), Tulsa, OK: Society of Economic Paleontologists and Mineralogists. <https://doi.org/10.2110/pec.88.01.0039>
- Vörösmarty, C. J., Syvitski, J., Day, J., de Sherbinin, A., Giosan, L., & Paola, C. (2009). Battling to save the World's River Deltas. *Bulletin of the Atomic Scientists*, *65*(2), 31–43. <https://doi.org/10.2968/065002005>
- Walling, D. E., & Webb, B. W. (1996). Erosion and sediment yield: A global overview. *IAHS Publications-Series of Proceedings and Reports-Intern Assoc Hydrological Sciences*, *236*, 3–20.
- Wang, H., Wu, X., Bi, N., Li, S., Yuan, P., Wang, A., et al. (2017). Impacts of the dam-orientated water-sediment regulation scheme on the lower reaches and delta of the Yellow River (Huanghe): A review. *Global and Planetary Change*, *157*, 93–113. <https://doi.org/10.1016/j.gloplacha.2017.08.005>
- Wong, M., & Parker, G. (2006). One-dimensional modeling of bed evolution in a gravel bed river subject to a cycled flood hydrograph. *Journal of Geophysical Research: Earth Surface*, *111*(3), 1–20. <https://doi.org/10.1029/2006JF000478>
- Wu, C., Nittrouer, J. A., Muto, T., Naito, K., & Parker, G. (2020). Morphodynamic equilibrium of lowland river systems during autoretreat. *Geology*, *48*(11), 1062–1066. <https://doi.org/10.1130/G47556.1>
- Yu, S.-Y., Törnqvist, T. E., & Hu, P. (2012). Quantifying Holocene lithospheric subsidence rates underneath the Mississippi Delta. *Earth and Planetary Science Letters*, *331–332*, 21–30. <https://doi.org/10.1016/j.epsl.2012.02.021>
- Zaitlin, B. A., Dalrymple, R. W., & Boyd, R. (1994). The stratigraphic organization of incised-valley systems associated with relative sea-level change. *Incised-Valley Systems: Origin and Sedimentary Sequences*. Special Publications of SEPM, (Vol. 51). SEPM Society for Sedimentary Geology. <https://doi.org/10.2110/pec.94.12.0045>
- Zhou, Y., Huang, H. Q., Nanson, G. C., Huang, C., & Liu, G. (2015). Progradation of the Yellow (Huanghe) River delta in response to the implementation of a basin-scale water regulation program. *Geomorphology*, *243*, 65–74. <https://doi.org/10.1016/j.geomorph.2015.04.023>